

Coherent interaction-free detection of microwave pulses with a superconducting circuit

Shruti Dogra, John J. McCord, and Gheorghe Sorin Paraoanu
*QTF Centre of Excellence, Department of Applied Physics,
Aalto University, FI-00076 Aalto, Finland*

(Dated: April 5, 2022)

We show that it is possible to ascertain the presence of a microwave pulse resonant with the second transition of a superconducting transmon circuit, while at the same time avoiding to excite the device onto the third level. In contrast to standard interaction-free measurement setups, where the dynamics involves a series of projection operations, our protocol employs a fully coherent evolution, which results, surprisingly, in a higher efficiency. Experimentally, this is done by using a series of Ramsey microwave pulses coupled into the first transition and monitoring the ground-state population.

INTRODUCTION

The interaction-free detection protocol [1] provides a striking illustration of the concept of negative-results measurements of Renninger [2] and Dicke [3]. The very presence of an ultrasensitive object in one of the arms of a Mach-Zehnder interferometer modifies the output probabilities even when no photon has been absorbed by the object. The detection efficiency can be enhanced by using the quantum Zeno effect through repeated no-absorption “interrogations” of the object [4–8] – a protocol which we will refer to as “projective”.

Here we describe and demonstrate experimentally a related effect that employs repeated coherent interrogations instead of projective ones. We implement a hypothesis-testing protocol where the task is to detect the presence of a microwave pulse in a transmission line using a resonantly-activated detector realized as a transmon three-level device. We require that at the end of the protocol the detector has not irreversibly absorbed the pulse, as witnessed by a non-zero population of the second excited state. Clearly this task cannot be achieved with a classical absorption-based detector (e.g. a bolometer) or by using a simple two-level system as detector. Our protocol is fundamentally different from the quantum Zeno interaction-free measurement: while in the latter case the mechanism of detection is the suppression of coherent evolution by projection on the interferometer path that does not contain the object, in our protocol the evolution of the state of the superconducting circuit remains fully coherent. Surprisingly, this coherent addition of amplitude probabilities results in a higher detection efficiency.

In our experiments, we realize a series of N Ramsey-like sequences by applying beam-splitter unitaries S_N to the lowest two energy levels of a superconducting transmon. This creates the analog of the standard Mach-Zehnder spatial setup in a time-domain configuration [9]. The microwave pulses of strength θ_j that we wish to detect – which we will refer to as B -pulses – couple resonantly into the next higher transition, see Fig. 1. Specifically, let us denote the first three levels of the transmon by $|0\rangle$, $|1\rangle$, and $|2\rangle$ and the asymmetric Gell-Mann

generators of $SU(3)$ by $\sigma_{kl}^y = -i|k\rangle\langle l| + i|l\rangle\langle k|$, with $k, l \in \{0, 1, 2\}$. Microwave pulses applied resonantly to the 0-1 and 1-2 transitions respectively result in unitaries $S_N = \exp[-i\pi\sigma_{01}^y/2(N+1)]$ and $B(\theta_j) = \exp(-i\theta_j\sigma_{12}^y/2)$ [10]. The protocol employs a series of $j = \overline{1, N}$ Ramsey segments, each containing a B -pulse with arbitrary strength θ_j , producing overall the evolution $U_N = \prod_{j=1}^N [S_N B(\theta_j)] S_N = S_N \prod_{j=1}^N [B(\theta_j) S_N]$. Note that the absence of B -pulses results in $[S_N]^{N+1} = -i\sigma_{01}^y + |2\rangle\langle 2|$, acting nontrivially only on the subspace $|0\rangle, |1\rangle$ – therefore at the end of the sequence the entire ground-state population is transferred onto the first excited state $|0\rangle \rightarrow |1\rangle$. The goal is to ascertain the presence of B -pulses without absorbing them, that is, without creating excitations on the level $|2\rangle$ of the transmon.

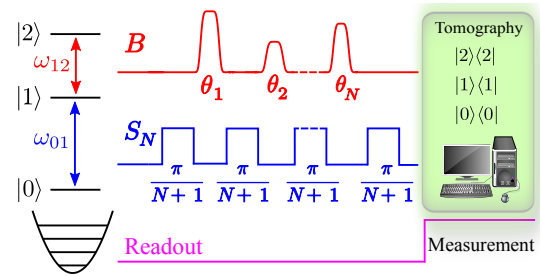


FIG. 1. Schematic showing our protocol, where S_N and B microwave pulses are shown in blue and red, respectively, along with the probe pulse for readout.

To understand the interaction-free physics in this setup, consider first a single sequence $N = 1$. The transmon is initialized in the ground state $|0\rangle$, which, when acted upon by S_1 ($\pi/2$ rotation around the y -axis in the $\{|0\rangle, |1\rangle\}$ subspace, corresponding to a $0.5 : 0.5$ beam-splitter), drives the qubit into a coherent equal-weight superposition state $(|0\rangle + |1\rangle)/\sqrt{2}$. Next, the application of $B(\theta)$ (here we take $\theta_1 \equiv \theta$) and the subsequent application of S_1 results in the state $S_1 B(\theta) S_1 |0\rangle = \sin^2(\theta/4) |0\rangle + \cos^2(\theta/4) |1\rangle + (1/\sqrt{2}) \sin(\theta/2) |2\rangle$, while if $B(\theta)$ is not present the final state is $|1\rangle$. By measuring dispersively the state of the transmon and finding it in the

state $|0\rangle$, we can ascertain the presence of the B pulse without irreversibly absorbing it. The final measurement results in this scheme are the populations p_0 (the fraction of pulses detected in an interaction-free manner), p_1 (the fraction of inconclusive outcomes), and p_2 (the probability of $B(\theta)$ absorption). For the ideal dissipationless case we have $p_0(\theta) = \sin^4(\theta/4)$, $p_1(\theta) = \cos^4(\theta/4)$ and $p_2(\theta) = (1/2)\sin^2(\theta/2)$. For $\theta = \pi$ this implies that we have $p_0(\pi) = 25\%$ chance of detecting the B -pulse without absorption, leaving $p_2(\pi) = 50\%$ as the probability of failure. As a key figure of merit we can define the Positive Ratio, $\text{PR}(\theta) = p_0(\theta)/[p_0(\theta) + p_1(\theta)]$, which reflects the efficiency with which the interaction-free detection of $B(\theta)$ is achieved *strictly speaking* without irreversible absorption. Its counterpart is the Negative Ratio, $\text{NR}(\theta) = p_1(\theta)/[p_0(\theta) + p_1(\theta)]$, the fraction of experiments that are not accompanied by $B(\theta)$ absorption, but for which we can not ascertain whether a B -pulse was present or not. These are the same figures of merit as in the projective case (see Supplementary Notes 1 and 2) [10].

RESULTS

In the experiments we use a transmon circuit with a dispersive readout scheme that allows us to measure simultaneously the populations of the first three levels. The 0-1 and 1-2 transitions are driven by two pulsed microwave fields, implementing respectively the S_N unitaries and the B -pulses. Details of simulations and a description of the experimental setup are presented in Methods.

Single B -pulse ($N = 1$)

The results for the the $N = 1$ interaction-free detection are shown in Fig. 2 and Fig. 3. Fig. 2(a) presents the populations p_0 , p_1 , and p_2 obtained experimentally, as well as a comparison with the simulated values and the ideal case. First, one notices that the results are not invariant under $\theta \rightarrow \theta + 2\pi$, which is intrinsically related to the lack of invariance of spin-1/2 states under 2π rotations. Indeed, $B(\theta + 2\pi) = \exp(-i\pi\sigma_{12}^y)B(\theta)$ acts by changing the sign of the probability amplitudes on the subspace $\{|1\rangle, |2\rangle\}$, which subsequently alters the interference pattern after the second beam-splitter unitary. Then, we see that at $\theta = \pi, 3\pi$ the experimentally obtained probability for the interaction-free detection is 0.26; the same would be expected also in the projective case [1, 10]. From Fig. 2 we also notice that at $\theta = 2\pi$ the probability p_0 reaches a maximum (1 in the ideal case), while p_1 and p_2 are minimized (zero in the ideal case). This happens also if beam-splitters with y -axis rotation angles other than $\pi/2$ are used. It is a situation that has no classical analog: we are able to detect with almost certainly a pulse that does not

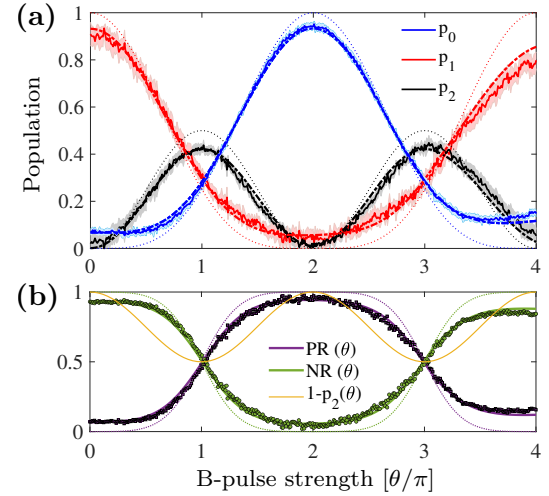


FIG. 2. (a) Populations vs. strength for a single B -pulse in our three-level system. The experimentally averaged profiles for ground state, first excited state and second excited states are represented by blue, red and black colored continuous lines. The corresponding colored dot-dashed lines are the simulated curves including decoherence and pulse imperfections, while the thin dotted lines show the ideal case. Each experimental curve is accompanied by a shaded region presenting the standard deviation of the mean obtained from 16 replicas of the same experiment. (b) Corresponding to each B -pulse strength, $\text{PR}(\theta) = p_0(\theta)/[p_0(\theta) + p_1(\theta)]$ and $\text{NR}(\theta) = p_1(\theta)/[p_0(\theta) + p_1(\theta)]$ obtained from the experiment are shown with purple circular markers and green square markers respectively, closely followed by the simulated purple and green continuous curves. The thin dotted lines represent the respective ideal cases, with no decoherence and without any experimental imperfections. The continuous yellow curve stands for the norm of the system subspace: $p_0(\theta) + p_1(\theta) = 1 - p_2(\theta)$.

change at all the populations. Indeed, as we can see from Fig. 2, the lesser of real transfer effect the pulse has, the better the efficiency is – a situation which is opposite to what we would expect intuitively from absorption-based detectors. As we will see next, when generalizing this result to $N > 1$ pulses, this maximum at $\theta = 2\pi$ extends to form a plateau of large p_0 values.

We can further characterize the sensing capabilities of the device by constructing the histograms in Fig. 3 for the presence/absence of a $\theta = \pi$ B -pulse and extracting the associated confusion matrix. Using standard terminology in hypothesis testing, positive/negative refer here to the presence/absence of the B -pulse, either predicted or real, and we eliminate the cases when the pulse is absorbed. The elements of the confusion matrix (Fig. 3) are: the True Positive Ratio $\text{TPR} = p_0(\theta = \pi)/(p_0(\theta = \pi) + p_1(\theta = \pi)) = \text{PR}(\pi)$, which is the measure of correct detection of the π B -pulse when it is applied, the False Positive Ratio $\text{FPR} = p_0(\theta = 0)/(p_0(\theta = 0) + p_1(\theta = 0)) = \text{PR}(0)$, which is the measure of incorrect detection of the B -pulse when it is not applied, the True Negative Ratio $\text{TNR} = p_1(\theta = 0)/(p_0(\theta = 0) + p_1(\theta = 0)) = \text{NR}(0)$, which is the correct non-

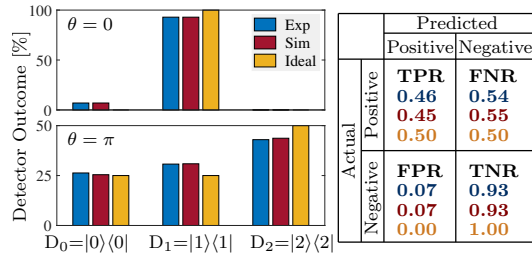


FIG. 3. (left panels) Histogram of events recorded by the detectors D_0 , D_1 , and D_2 , which are constructed as projectors. The results are obtained from 10^6 realizations of the experiment, and for B -pulse strengths $\theta = 0, \pi$. The percentage outcome at D_0 corresponds to successful interaction-free detection, D_2 represents the number of times the pulse is absorbed, and D_1 are the inconclusive instances. (right panel) Confusion matrix for $\theta = \pi$, showing the experimental (blue), simulated (red) and ideally expected (yellow) ratios.

detection of the B -pulse when it is not applied, and the False Negative Ratio $FNR = p_1(\theta = \pi)/(p_0(\theta = \pi) + p_1(\theta = \pi)) = NR(\pi)$, which is the incorrect non-detection of the B -pulse when it is applied.

Two consecutive B -pulses ($N = 2$)

Next, we use our superconducting circuit to realize the coherent interaction-free detection of $N = 2$ pulses. Note that the equivalent projective case [4, 5] for $N > 1$ would need to employ the quantum Zeno effect to confine the dynamics in the $|0\rangle, |1\rangle$ subspace. This would require the monitoring the state $|2\rangle$ and postselection, resulting in a non-unitary dynamics. Different from this, in our protocol quantum coherence serves as a resource, yielding significantly higher detection efficiency. The enhancement can be understood as the coherent accumulation of amplitude probabilities on the state $|0\rangle$ under successive interactions with the B -pulse and applications of Ramsey S_N (see Supplementary Note 3) [10]. This unexpected effect can be seen already for $N = 2$, where a straightforward calculation for the ideal case and $\theta_1 = \theta_2 = \pi$ yields probabilities $p_0 = 0.8091$, $p_1 = 0.0034$, $p_2 = 0.1875$, and $PR = 0.99$, while the equivalent respective figures for the projective case are 0.4219, 0.1406, 0.4375, and 0.75.

Further, we experimentally realize a general case where B -pulse strengths are different, *i.e.* $\theta_1, \theta_2 \in [0, 4\pi]$. Experimental and simulated results for the ground state, first excited state and second excited state populations as functions of θ_1 and θ_2 are shown in Fig. 10(a,b,c) respectively. The Positive Ratio $PR(\theta_1, \theta_2) = p_0(\theta_1, \theta_2)/(p_0(\theta_1, \theta_2) + p_1(\theta_1, \theta_2))$ and the Negative Ratio $NR(\theta_1, \theta_2) = p_1(\theta_1, \theta_2)/(p_0(\theta_1, \theta_2) + p_1(\theta_1, \theta_2))$ as a function of θ_1 and θ_2 are shown in Fig. 5. Experimental and simulated results are in very good agreement with each other.

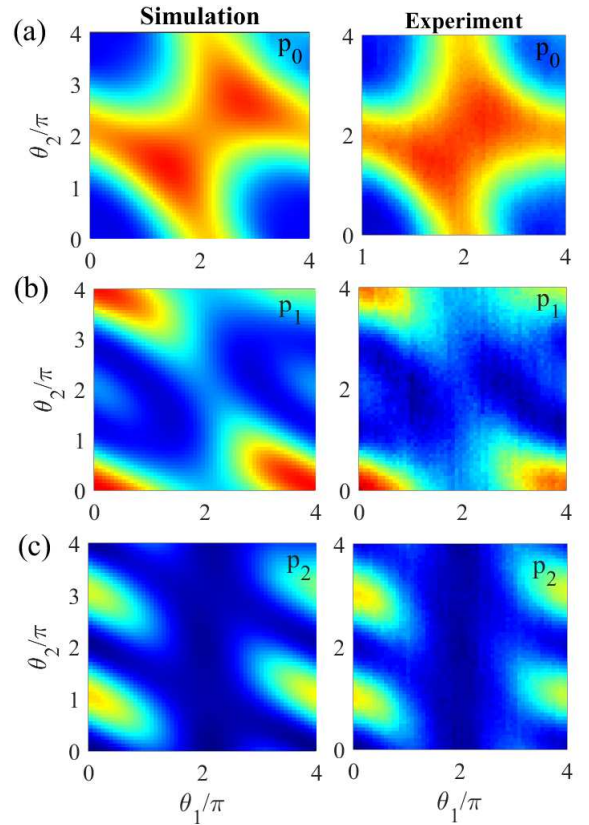


FIG. 4. 2D population maps for (a) ground, (b) first excited, and (c) second excited state populations as a function of B -pulse strengths θ_1 and θ_2 .

Multiple consecutive B -pulses ($N > 2$)

Next, we use our superconducting circuit to realize the coherent interaction-free detection of $N > 2$ pulses, where we observe even more efficient coherent accumulation of amplitude probabilities on the state $|0\rangle$ under successive interactions with the B -pulse and applications of Ramsey S_N [10]. In the coherent case, values $p_0 > 90\%$ are reached already for $N \geq 3$, while in the projective case they are reached only for $N \geq 23$.

In the experiments we use both equal-strength pulses $\theta_j = \theta$ and pulses with randomly-chosen $\theta_j \in \{0, \pi\}$, $j = 1, N$, while the beam-splitter unitary is a $\pi/(N+1)$ rotation around the y axis in the $\{|0\rangle, |1\rangle\}$ subspace. To recall, in the absence of the B -pulses we have $[S_N]^{N+1}$ and in the presence of the B -pulses we have $S_N \prod_{j=1}^N [B(\theta_j) S_N]$.

The large- N experimental sequences have a significant time cost with the worst case of 25 B -pulses corresponding to $4.3 \mu\text{s}$, which is even longer than the relaxation time $\Gamma_{10}^{-1} = 3.4 \mu\text{s}$ (see Methods for details). Thus, in addition to the standard three-level Lindblad master equation [11, 12], in order to accurately model the system we may include a depolarization channel $\rho(t) \rightarrow (1 - \epsilon)\rho(t) + \epsilon\mathbb{I}_3/3$ [34] (see Methods). Here we assume

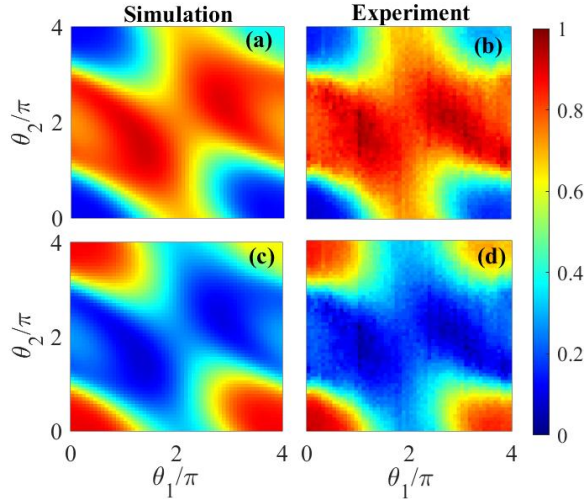


FIG. 5. (a,c) Simulated and (b,d) experimental 2D maps for the (a,b) Positive Ratio $PR(\theta_1, \theta_2)$ and the (c,d) Negative Ratio $NR(\theta_1, \theta_2)$ as a function of θ_1 and θ_2 .

that the imperfections in the 1–2 drive results in mixing of the qutrit state; hence the parameter ϵ is taken as directly proportional to the pulse amplitude, given by $\epsilon[\theta] = 1.8 \times 10^{-3} \times \theta/\pi$. This choice of model fits our experimental data very well as shown in Fig. 6, where continuous lines correspond to the simulation including depolarizing channel and dotted lines correspond to simulation without the depolarizing channel. As expected, the overall effect of depolarization is more prominent for a larger number of B -pulses and for large θ . In all of these plots, experimental results are shown by markers with experimental error bars (standard deviation about the mean by four repetitions of the same experiment). Small deviations of the experimental values from the ideal results are due to decoherence and pulse errors. Larger values of p_0 correspond to a higher probability of interaction-free detection. We have verified numerically that with increasing N , p_0 increases, approaching 1 in an ideal case.

In the case of equal-strength pulses, for each N , we perform a total of \mathcal{M} experiments, with the B -pulse strength varying linearly with the experiment number as: $\theta = \theta_{j,m} = m\pi/\mathcal{M}$ with labels: $j = \overline{1, N}$ and $m = \overline{1, \mathcal{M}}$ such that $\theta \in [0, \pi]$. The results for the overall efficiency p_0 are shown in Fig. 6(a), for various numbers $N \in [1, 25]$ of B -pulses and $\mathcal{M} = 200$. Simulated and experimental p_0 values are shown as surface plots in parts (i) and (ii) respectively.

Interestingly, with increasing number of B -pulses, the final p_0 is independent of the B -pulse strength (θ), and has a tendency to reach large values. As anticipated, a plateau characterized by high efficiency is formed, which is the extension to smaller θ 's of the maximum seen in the $N = 1$ case around $\theta = 2\pi$. This is also clearly reflected from the plot in Fig. 6(a)(iii) showing the mean value of

p_0 ($E[p_0]$ in red) resulting from experiments with different B -pulse strengths versus the number of Ramsey sequences. The ‘no B -pulse’ situation is shown with black square markers and that of maximum B -pulse strength is shown with blue triangular markers, where the increase in $p_0(\theta = 0)$ with N and lower values of $p_0(\theta = \pi)$ is due to the decoherence. It is clear from the three curves that $E[p_0]$ tends to approach the higher limiting values, which is attributed to the larger plateau of high efficiency with increasing N (see Supplementary Fig. 13)[10]. As a direct consequence of the plateau formation, the minimum value of θ that gives rise to near maximal p_0 is much smaller than π for large N . The standard deviation of the p_0 distribution versus N is shown in Fig. 6(a)(iv). Each of these experimental values are accompanied by simulations, demonstrating quite close agreement. A comparison (see Supplementary Notes 2 and 3)[10] with the projective case - for which exact analytical results are available - demonstrates the advantage of the coherent protocol for all values of N .

We also study the case of randomly-chosen $\theta_j \in [0, \pi]$, $j = \overline{1, N}$, with results shown in Fig. 6(b). Panels (i), (ii) present surface maps of the simulated and experimental p_0 versus N and m , where $\mathcal{M} = 400$. Experimental and simulated mean- $E[p_0]$, minimum- $p_0^{(\min)}$, and maximum- $p_0^{(\max)}$ values obtained from this distribution are shown in panel (iii) with markers and continuous curves respectively. The standard deviation $\sigma[p_0] = \sqrt{E[(p_0 - E[p_0])^2]}$ of p_0 versus N is shown in part (iv). Again, we observe that the mean value of ground state population increases with N , while the standard deviation of repeated measurements decreases with N . Thus, for a large N , the B -pulse strength does not matter anymore, and we obtain a highly efficient interaction-free detection. Surprisingly, the case with random B -pulse strengths appears to outperform the case with identical B -pulses. Comparing parts (a)(iii) and (b)(iii) of Fig. 6, the efficiency of the coherent interaction-free detection in the worst case (green curve) for random B -pulse strengths is already high enough, with a maximum value (for $N = 25$) of 0.83 ± 0.03 (experiment) and 0.82 (simulation), close to the mean values $E[p_0] = 0.88 \pm 0.03$ (experimental) and $E[p_0] = 0.87$ (simulated). On the other hand, in the case of identical B -pulses, the maximum values reached are only $E[p_0] = 0.81 \pm 0.01$ (experiment) and $E[p_0] = 0.80$ (simulation), even slightly below the worst-case scenario with random pulses. Also, especially at large N 's, the standard deviation about the mean value of the distribution is much lower in the case of random B -pulses as opposed to the identical B -pulses case, which is clear upon comparison of Fig. 6(a)(iv) and b(iv). Thus, an adversarial attempt to randomize the B -pulse strengths in order to evade detection has, surprisingly, the opposite effect, improving the interaction-free coherent detection.

Finally, in Fig. 6(c) we present some of the p_0 distri-

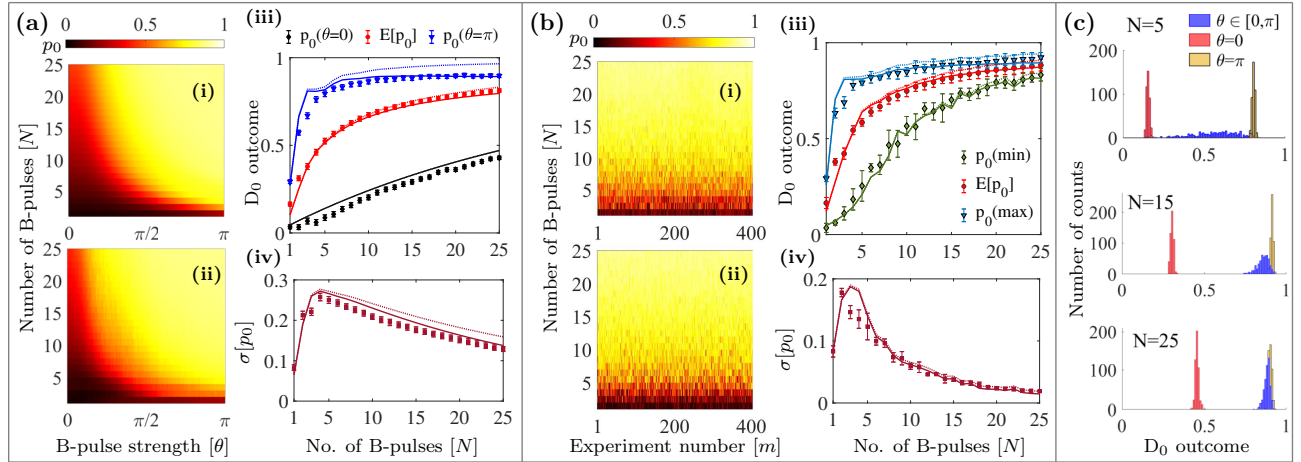


FIG. 6. Results for the D_0 outcome in the case of multiple Ramsey sequences with B -pulses ($N \in [1, 25]$) of varying strengths, $\theta_{j,m} \in [0, \pi]$ with $j = 1, N$ and m indexing the experimental realization for a given N . (a) Plots for identical B -pulses $\theta_{j,m} = \theta = m\pi/M$ for a given N : (i) Simulated and (ii) experimentally obtained maps (iii) Values of p_0 at extreme B -pulse strengths ($\theta = 0, \pi$) and mean p_0 ($E[p_0]$) versus N with markers with error bars showing the experimental results and the corresponding continuous lines obtained from the simulations. Red circular markers present the mean value $E[p_0]$, black diamond markers correspond to the case with no B -pulses ($\theta = 0$) and data points with blue triangular markers stand for the case of maximum B -pulse strengths ($\theta = \pi$). (iv) Standard deviation evaluated for a given N versus N . (b) Plots for arbitrarily chosen (i)-(iv) $\theta_{j,m} \in [0, \pi]$. (i), (ii) are the simulated and experimental maps of p_0 as a function of N and m , (iii) Simulated (continuous lines) and experimental (markers with error bars) of mean and extremum values, and (iv) standard deviation of p_0 versus N . Dotted curves in all the plots are simulations without the inclusion of depolarization. (c) The experimental ground state population counts for various system sizes ($N = 5, 15, 25$) with B -pulses of arbitrary strengths, $\theta \in [0, \pi]$ compared with those of extreme B -pulse strengths: $\theta = \pi$ and $\theta = 0$ (no B -pulse). Clearly as the system size increases, the strengths of the B -pulses become less significant and approach the population clustering near the maximal p_0 , which is a signature of the highly efficient interaction-free detection.

butions for $N = 5, 15, 25$, where the red colored distribution in all three cases corresponds to $\theta_j = \theta = 0$ – and hence lie at the lower limit of p_0 range, while the distribution in yellow represents the case $\theta_j = \theta = \pi$ and lies close to the upper limit. The interesting part is the distribution in blue with arbitrarily chosen B -pulse strengths $\theta_j = \theta \in [0, \pi]$, which moves towards the right side and tends to squeeze with increasing N . The same idea is conveyed by the increasing mean value ($E[p_0]$) and decreasing standard deviation with N as discussed earlier.

The coherent interaction-free protocol can also be represented in time-domain on the Majorana sphere [14, 15]. The system starts with both Majorana stars at the North Pole. In the absence of the B -pulses, it ends with one star at the North Pole and the other at the South Pole. In the presence of the B -pulses with $\theta_j = \pi$, both stars are located in the northern hemisphere for $N \geq 2$, and they tend to get closer and closer to the North Pole with increasing N (see Supplementary Note 6) [10].

CONCLUSIONS AND PERSPECTIVES

In conclusion, we proposed a coherent interaction-free process for the detection of microwave pulses and we realized it experimentally with a superconducting quantum circuit. For the case of a single pulse with strength $\theta = \pi$,

we obtain an interaction-free detection probability of 0.26. Further, we have emulated multiple Ramsey sequences and we obtained a highly efficient interaction-free detection of the B -pulse approaching unity. We observe that for a large number of sequences a high detection probability is obtained irrespective to the strength of the pulses, and, surprisingly, this probability is even higher when the pulses have random strength. Our results can be applied for non-invasive monitoring of microwave currents and pulses, which is an outstanding problem in quantum simulation [16]. They provide a proof of concept for a photon detector, conceptually and practically different from realizations based on cavity-assisted conditional gates [17, 18]. The protocol works also when the B -pulse is a Fock state and it can be utilized to assess non-destructively the presence of photons stored in superconducting cavities (see Supplementary Note 1) [10]. This can be utilized for axion detection, where the generation of a photon is expected to be a rare event and also the existing detectors have a high dark count rate: thus, one can increase the confidence level by assessing its presence first non-destructively and then confirm it by more conventional means. This concept can be implemented in other experimental platforms where a three-level system is available. Projective interaction-free measurements have found already applications in optical imaging [19], counterfactual communication [7, 20–24], ghost-

imaging [25, 26], cryptographic key distribution [27, 28], and measurement-driven engines [29]; we expect that our coherent version will be similarly adapted to these nascent fields.

METHODS

Experimental Setup

A schematic of the setup is shown in Fig. 7. The sample is mounted in a dilution refrigerator via a sample holder which is thermally anchored to the mixing chamber. There are several lines which connect our sample to the external circuitry: the microwave gate line which delivers the microwave drive pulses to the transmon, a flux-bias line which provides a constant DC magnetic field, and the measurement line which is capacitively coupled to the readout resonator via an input/output capacitor. The flux-bias line sends a current near the SQUID loop, which induces a magnetic flux and thus enables the transmon transition frequency to be tuned. The transmission line is used to probe the resonator by sending microwave pulses or continuous signals into it.

The drive pulses used to realize the beam-splitter unitaries and the B -pulses have super-Gaussian envelopes ($\propto \exp[-(t/\tau)^4/2]$) with the following time-dependence:

$$\Omega(t) = \Omega_0 \exp \left[-\frac{1}{2} \left(\frac{t}{\tau} \right)^4 \right], \quad (1)$$

where $\Omega_0^{(S_N)} = \pi / [(N+1) \int_{-\tau_c}^{\tau_c} \exp[-(t/\tau)^4/2] dt]$ for beam-splitters and $\Omega_0(\theta) = \theta / \int_{-\tau_c}^{\tau_c} \exp[-(t/\tau)^4/2] dt$ for the B -pulses. Thus, the effective pulse area is determined by $\int_{-\tau_c}^{\tau_c} \exp[-(t/\tau)^4/2] dt$, where $\pm\tau_c$ are the start and the end points of the drive pulse (the points where the pulse is truncated) and τ is a time constant. In our experiments $\tau = 14$ ns and $\tau_c = 2\tau = 28$ ns, which corresponds to a total pulse length of 56 ns and an effective pulse area $\int_{-\tau_c}^{\tau_c} \exp[-(t/\tau)^4/2] dt = 30.18$ ns. The amplitude Ω_0 is determined from Rabi oscillations measurements varying the amplitude of the transmon drive pulse and its frequency while keeping the pulse duration fixed. The variation of the pulse amplitude is achieved using I and Q waveform amplitudes from our arbitrary waveform generator (AWG), which are mixed in an IQ mixer with the LO tone generated by a continuous microwave generator (AWG). We utilize a homodyne detection scheme for determining the state of the transmon. A microwave source (PNA) provides a continuous signal at the LO frequency for our readout pulse as well as that for the demodulated reflected signal from the resonator. As such, a power splitter is employed to halve this signal, where one part is sent to the LO port of an IQ mixer which modulates a probe pulse with readout rectangular envelopes from the I and Q quadratures generated by the AWG. The other

part is sent to an IQ mixer which demodulates the signal reflected back from the resonator. After demodulation the quadratures of this mixer are amplified and subsequently digitized and recorded via our data acquisition card.

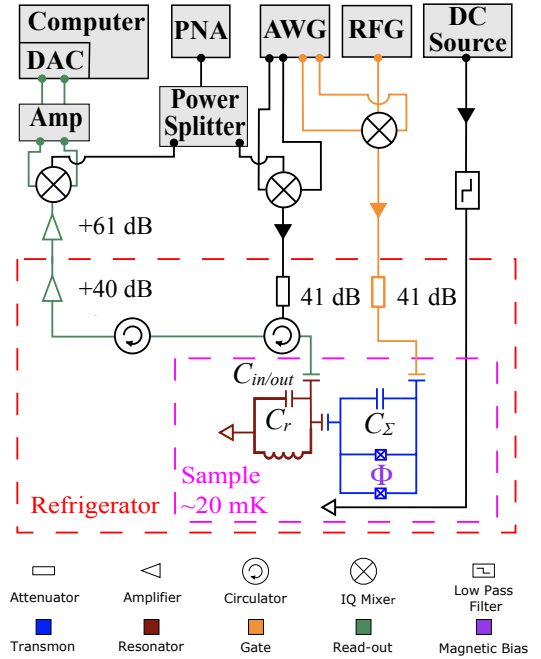


FIG. 7. Schematic of the experimental setup used in this work, including the transmon circuit's integration with the dilution refrigerator and microwave electronics.

Decoherence model and numerical simulations

In the rotating wave approximation (RWA), the transmon Hamiltonian in the three-level truncation is

$$H(t) = \frac{\hbar}{2} \left[\Omega_{01}(t) e^{i\phi_{01}} |0\rangle\langle 1| + \Omega_{01}(t) e^{-i\phi_{01}} |1\rangle\langle 0| + 2\delta_{01} |1\rangle\langle 1| \right] + \frac{\hbar}{2} \left[\Omega_{12}(t) e^{i\phi_{12}} |1\rangle\langle 2| + \Omega_{12}(t) e^{-i\phi_{12}} |2\rangle\langle 1| + 2(\delta_{01} + \delta_{12}) |2\rangle\langle 2| \right], \quad (2)$$

where the drive amplitudes follow the form as per Eq. (1), and are denoted as $\Omega_{01}(t)$ and $\Omega_{12}(t)$ for the $|0\rangle - |1\rangle$ and $|1\rangle - |2\rangle$ transitions respectively, carrying the respective phase factors $e^{\pm i\phi_{01}}$ and $e^{\pm i\phi_{12}}$ [12]. With the notation $\sigma_{kl} = |k\rangle\langle l|$, and assuming resonance $\delta_{01} = \delta_{12} = 0$, the Hamiltonian reads

$$H(t) = \frac{\hbar\Omega_{01}(t)}{2} e^{i\phi_{01}} \sigma_{01} + \frac{\hbar\Omega_{12}(t)}{2} e^{i\phi_{12}} \sigma_{12} + \text{h.c.} \quad (3)$$

To introduce dissipation, we use the standard Lindblad master equation, where $D[L]\rho = L\rho L^\dagger - \frac{1}{2}\{L^\dagger L, \rho\}$ is the Lindblad super operator and L is the jump operator applied to the density matrix ρ . For our three-level system

we have (see *e.g.* [30, 31])

$$\dot{\rho} = -\frac{i}{\hbar}[H, \rho] + \sum_{k,l=0,1,2}^{k \neq l} \Gamma_{k-l} D[\sigma_{lk}] \rho + \sum_{k=0,1,2} \frac{\Gamma_k^\phi}{2} D[\sigma_{kk}] \rho,$$

where Γ_{k-l} is the excitation/decay rate between states $|k\rangle$ and $|l\rangle$, and Γ_k^ϕ is the dephasing rate associated with level k . The operators $\sigma_{lk} = |l\rangle\langle k|$ with $k > l$ are lowering operators and those with $k < l$ are raising operators corresponding to the transition lk . The Lindblad dephasing operators act only on the off-diagonal matrix elements, while the relaxation operators act on both the diagonal and off-diagonal matrix elements. However, since we operate on transitions, the individual dephasing rates Γ_k^ϕ cannot be determined directly from experiments. Instead, we can rewrite the equation above in a form that involves only pairs of levels [12]

$$\begin{aligned} \dot{\rho} = & -\frac{i}{\hbar}[H, \rho] + \Gamma_{2-1}\rho_{22}(\sigma_{11} - \sigma_{22}) + \Gamma_{1-0}\rho_{11}(\sigma_{00} - \sigma_{11}) \\ & + \Gamma_{1-2}\rho_{11}(\sigma_{22} - \sigma_{11}) + \Gamma_{0-1}\rho_{00}(\sigma_{11} - \sigma_{00}) \\ & - \sum_{k,l=0,1,2}^{k \neq l} \gamma_{kl} \rho_{kl} \sigma_{kl}, \end{aligned}$$

where the relaxation rates satisfy the detailed balance condition $\Gamma_{k-l} = e^{-\hbar\omega_{kl}/k_B T} \Gamma_{l-k}$ (with $l > k$) at a temperature T with k_B as the Boltzmann constant and $\hbar\omega_{kl}$ being the energy level spacing between the k^{th} and l^{th} levels. By introducing the occupation numbers $n_{kl} = 1/[\exp(-\hbar\omega_{kl}/k_B T) - 1]$, the rates Γ_{k-l} can be expressed in terms of the zero-temperature decay rates Γ_{lk} (with $l > k$) as $\Gamma_{k-l} = n_{kl} \Gamma_{lk}$ ($l > k$) and $\Gamma_{l-k} = (n_{kl} + 1) \Gamma_{lk}$ ($l > k$). It is clear from this decoherence model that the relaxation rates Γ_{k-l} for $k < l$ are significant only at higher temperatures of several tens of mK, which lead to transitions from lower to higher energy levels. The decay rates for the off-diagonal matrix elements are $\gamma_{10} = \gamma_{01} = (\Gamma_{1-0} + \Gamma_{0-1})/2 + \Gamma_{10}^\phi$, $\gamma_{21} = \gamma_{12} = (\Gamma_{1-2} + \Gamma_{2-1})/2 + \Gamma_{21}^\phi$, and $\gamma_{20} = \gamma_{02} = (\Gamma_{1-0} + \Gamma_{2-1} + \Gamma_{0-1} + \Gamma_{1-2})/2 + \Gamma_{20}^\phi$. Here we define the dephasing rates associated with each transition as $\Gamma_{kl}^\phi = \Gamma_{lk}^\phi = (\Gamma_k^\phi + \Gamma_l^\phi)/2$. Note that the off-diagonal decay of the matrix elements ρ_{kl} due to dephasing can be understood as resulting from $\mathbb{I}_{kl} D[\sigma_{kl}^z] \rho \mathbb{I}_{kl} = \sigma_{kl}^z \rho \sigma_{kl}^z - \mathbb{I}_{kl} \rho \mathbb{I}_{kl}$, which is the familiar qubit dephasing expression projected onto the $\{|k\rangle, |l\rangle\}$ subspace, with $\sigma_{kl}^z = \sigma_{kk} - \sigma_{ll} = |k\rangle\langle k| - |l\rangle\langle l|$ and $\mathbb{I}_{kl} = \sigma_{kk} + \sigma_{ll} = |k\rangle\langle k| + |l\rangle\langle l|$.

Experimental parameters and sample specifications

For the $N = 1$ and $N = 2$ cases, experiments have been performed on a sample with $|0\rangle - |1\rangle$ and $|1\rangle - |2\rangle$ transition frequencies being $\omega_{01}/(2\pi) = 5.01$ GHz and $\omega_{12}/(2\pi) = 4.65$ GHz respectively. The simulations make use of the general form of the Lindblad master equation for the quantum state evolution with relaxation and dephasing rates

obtained from standard characterization measurements: $\Gamma_{10} = 0.72$ MHz, $\Gamma_{21} = 1.55$ MHz, $\Gamma_{10}^\phi = 0.4$ MHz, $\Gamma_{21}^\phi = 0.6$ MHz, and $\Gamma_{02}^\phi = 1$ MHz. The duration of the beam splitter pulse is 56 ns (see also Eq. 1) and the amplitude of the pulse is directly proportional to the angle of rotation (in a given subspace). The B -pulses however have a fixed duration of 56 ns until $\theta = 3.38\pi$, beyond which the upper limit of the output power from our arbitrary waveform generator (AWG) is reached. To tackle this issue, the pulse duration is gradually increased from 56 ns to 61 ns in steps of 1 ns (as θ varies from 3.38π to 4π), such that the desired pulse-area is attained with lower pulse amplitudes. The transmon starts in thermal equilibrium at an effective temperature of 50 mK (measured independently, see [32]) such that the initial probability of occupation of the ground state, first excited state and second excited state is $p_0 = 0.9917 = 99.17\%$, $p_1 = 0.0082 = 0.82\%$, and $p_2 = 0.0001 = 0.1\%$.

For experiments involving a large number of pulses ($N > 2$) we use a sample with $\omega_{01}/(2\pi) = 7.20$ GHz and $\omega_{12}/(2\pi) = 6.85$ GHz. The relaxation and dephasing rates obtained from independent measurements are $\Gamma_{10} = 0.29$ MHz, $\Gamma_{21} = 1.15$ MHz, $\Gamma_{10}^\phi = 0.18$ MHz, $\Gamma_{21}^\phi = 1.82$ MHz, and $\Gamma_{02}^\phi = 1.70$ MHz. All the beam splitter pulses are 56 ns and B -pulses are of duration 112 ns with various different amplitudes. For the case of identical B -pulses, θ is increased linearly from 0 to π in 200 steps and in each case p_0 is measured for $N \in [1, 25]$. To obtain the error bars, each experiment is repeated four times. In the case of random B -pulses, random strengths are chosen arbitrarily from an uniform distribution of random numbers from 0 to π . Error bars result from the four repetitions of the same experiment. The corresponding surface maps, histograms and mean and standard deviation values are presented and discussed in the main text. For further details on the errors due to pulse imperfections, see Supplementary Note 5 [10].

For very long experiments, it is known that we can accumulate errors resulting in excess populations on the higher energy levels. The standard description for this effect is via an additional depolarizing channel [34]. For a three-level system the depolarizing channel can be written in the operator-sum representation [33], which is a completely positive trace-preserving map, such that the final state is given by

$$\rho_f = \sum_v K_v \rho K_v^\dagger, \quad \text{with} \quad \sum_v K_v^\dagger K_v = \mathbb{I}_3. \quad (4)$$

The Kraus operators K_v 's are given in terms of Gell-Mann matrices: $K_1 = \sqrt{\epsilon/6} \lambda_1$, $K_2 = \sqrt{\epsilon/6} \lambda_2$, $K_3 = \sqrt{\epsilon/6} \lambda_4$, $K_4 = \sqrt{\epsilon/6} \lambda_5$, $K_5 = \sqrt{\epsilon/6} \lambda_6$, $K_6 = \sqrt{\epsilon/6} \lambda_7$, $K_7 = \sqrt{\epsilon/3} \lambda_3$, $K_8 = \sqrt{\epsilon/6} (\sqrt{3} \lambda_8 - \lambda_3)$, $K_9 = \sqrt{\epsilon/6} (\sqrt{3} \lambda_8 + \lambda_3)$, and $K_{10} = \sqrt{1-8\epsilon/9} \mathbb{I}_3$. Here, $\lambda_{1(2)} = \sigma_{01}^{x(y)}$, $\lambda_{4(5)} = \sigma_{02}^{x(y)}$, $\lambda_{6(7)} = \sigma_{12}^{x(y)}$, $\lambda_3 = \sigma_{01}^z$, and $\lambda_8 = (\sigma_{02}^z + \sigma_{12}^z)/\sqrt{3}$. The final state following

Eq. (4) is

$$\rho_f = \frac{\epsilon \mathbb{I}_3}{3} + (1 - \epsilon) \rho. \quad (5)$$

In other words the system is replaced with the completely mixed state $\mathbb{I}_3/3$ with probability ϵ – otherwise it is unaffected, with probability $1 - \epsilon$. We are considering only the depolarization caused by the B -pulse, with a value $\epsilon = 1.8 \times 10^{-3}$ for a π pulse applied on the $|1\rangle - |2\rangle$ transition; this is obtained by a best-fit of the $\theta = \pi$ data. For arbitrary θ it is natural to consider a linear interpolation $\epsilon[\theta] = 1.8 \times 10^{-3} \times \theta/\pi$.

DATA AVAILABILITY

The data and codes that support the findings of this study are available from authors upon reasonable request.

AUTHOR CONTRIBUTIONS

SD and GSP conceived the idea and obtained key results. SD did the experiments and performed detailed analysis of the experimental data with inputs from JMC. SD and JMC did the simulations. All authors contributed to analytical calculations, discussed the results, and wrote the manuscript.

COMPETING INTERESTS

The authors declare no competing interests.

ACKNOWLEDGMENTS

We are grateful to Kirill Petrovnikin, Aidar Sultanov, Andrei Lebedev, Sergey Danilin, and Miika Haataja for assistance with sample fabrication and measurements. This project has received funding from the European Union’s Horizon 2020 research and innovation programme under grant agreement no. 862644 (FET-Open project QUARTET). We also acknowledge support from the Academy of Finland under the RADDESS programme (project 328193) and the Finnish Center of Excellence in Quantum Technology QTF (projects 312296, 336810). This work used the experimental facilities of the Low Temperature Laboratory and Micronova of OtaNano research infrastructure.

- [2] M. Renninger, *Zeitschrift für Physik* **136**, 251 (1953).
- [3] R. H. Dicke, *American Journal of Physics* **49**, 925 (1981).
- [4] P. Kwiat, H. Weinfurter, T. Herzog, A. Zeilinger, and M. A. Kasevich, *Phys. Rev. Lett.* **74**, 4763 (1995).
- [5] P. G. Kwiat, A. G. White, J. R. Mitchell, O. Nairz, G. Weihs, H. Weinfurter, and A. Zeilinger, *Phys. Rev. Lett.* **83**, 4725 (1999).
- [6] A. Peres, *Am. J. Phys.* **48**, 931 (1980).
- [7] L. Vaidman, *Journal of Physics A: Mathematical and Theoretical* **48**, 465303 (2015).
- [8] J. Peise, B. Lücke, L. Pezzé, F. Deuretzbacher, W. Ertmer, J. Arlt, A. Smerzi, L. Santos, and C. Klemp, *Nature Communications* **6**, 6811 (2015).
- [9] G. S. Paraoanu, *Phys. Rev. Lett.* **97**, 180406 (2006).
- [10] See Supplementary Information.
- [11] H. Breuer and F. Petruccione, *The theory of open quantum systems* (Oxford University Press, 2002).
- [12] K. S. Kumar, A. Vepsäläinen, S. Danilin, and G. S. Paraoanu, *Nature Communications* **7**, 10628 (2016).
- [13] M. A. Nielsen and I. L. Chuang, *Quantum Computation and Quantum Information* (Cambridge University Press, Cambridge UK, 2000).
- [14] E. Majorana, *Nuovo Cimento* **9**, 43 (1932).
- [15] S. Dogra, A. Vepsäläinen, and G. S. Paraoanu, *Phys. Rev. Research* **2**, 043079 (2020).
- [16] K. T. Geier, J. Reichstetter, and P. Hauke, arXiv:2106.12599 (2021).
- [17] S. Kono, K. Koshino, Y. Tabuchi, A. Noguchi, and Y. Nakamura, *Nature Physics* **14**, 546 (2018).
- [18] J.-C. Besse, S. Gasparinetti, M. C. Collodo, T. Walter, P. Kurpiers, M. Pechal, C. Eichler, and A. Wallraff, *Phys. Rev. X* **8**, 021003 (2018).
- [19] A. G. White, J. R. Mitchell, O. Nairz, and P. G. Kwiat, *Phys. Rev. A* **58**, 605 (1998).
- [20] H. Salih, Z.-H. Li, M. Al-Amri, and M. S. Zubairy, *Phys. Rev. Lett.* **110**, 170502 (2013).
- [21] Y. Cao, Y.-H. Li, Z. Cao, J. Yin, Y.-A. Chen, H.-L. Yin, T.-Y. Chen, X. Ma, C.-Z. Peng, and J.-W. Pan, *Proceedings of the National Academy of Sciences* **114**, 4920 (2017).
- [22] Y. Aharonov and L. Vaidman, *Phys. Rev. A* **99**, 010103 (2019).
- [23] I. A. Calafell, T. Strömberg, D. R. M. Arvidsson-Shukur, L. A. Rozema, V. Saggio, C. Greganti, N. C. Harris, M. Prabhu, J. Carolan, M. Hochberg, T. Baehr-Jones, D. Englund, C. H. W. Barnes, and P. Walther, *npj Quantum Information* **5**, 61 (2019).
- [24] Y. Aharonov, E. Cohen, and S. Popescu, *Nature Communications* **12**, 4770 (2021).
- [25] Y. Zhang, A. Sit, F. Bouchard, H. Larocque, F. Grenapin, E. Cohen, A. C. Elitzur, J. L. Harden, R. W. Boyd, and E. Karimi, *Opt. Express* **27**, 2212 (2019).
- [26] J. R. Hance and J. Rarity, *npj Quantum Information* **7**, 88 (2021).
- [27] T.-G. Noh, *Phys. Rev. Lett.* **103**, 230501 (2009).
- [28] Z.-H. Li, L. Wang, J. Xu, Y. Yang, M. Al-Amri, and M. S. Zubairy, *Phys. Rev. A* **101**, 022336 (2020).
- [29] C. Elouard, M. Waegell, B. Huard, and A. N. Jordan, *Foundations of Physics* **50**, 1294 (2020).
- [30] J. Li, M. A. Sillanpää, G. S. Paraoanu, and P. J. Hakonen, *Journal of Physics: Conference Series* **400**, 042039 (2012).
- [31] D. G. Tempel and A. Aspuru-Guzik, *Chemical Physics* **391**, 130 (2011), open problems and new solutions in time dependent density functional theory.

[1] A. C. Elitzur and L. Vaidman, *Foundations of Physics* **23**, 987–997 (1993).

[32] A. Sultanov, M. Kuzmanović, A. V. Lebedev, and G. S. Paraoanu, *Applied Physics Letters* **119**, 144002 (2021).

[33] K. Kraus, *States, Effects and Operations: Fundamental Notions of Quantum Theory, Lecture Notes in Physics Vol. 190* (Springer-Verlag, New York, 1983).

[34] M. A. Nielsen and I. L. Chuang, *Quantum Computation and Quantum Information* (Cambridge University Press, Cambridge UK, 2000).

[35] S. Dogra and G. S. Paraoanu, *AIP Conference Proceedings* **2362**, 03004 (2021).

**SUPPLEMENTARY INFORMATION:
COHERENT INTERACTION-FREE DETECTION OF MICROWAVE PULSES WITH A SUPERCONDUCTING CIRCUIT**

This supplement explores more thoroughly the coherent interaction-free measurements presented in this work, and discusses how our coherent interaction-free detection scheme compares with the standard projective non-unitary case typically realized in quantum optical systems [4]. In particular, we compare efficiencies for both schemes up to $N = 25$, and further compare these two cases when dissipation is applied via the Lindblad master equation. We also present general analytical expressions for arbitrary N in case of our coherent protocol and various simulations in support of our claims. An alternative analysis of the coherent interaction-free detection protocol is also presented by considering the quantization of the B-pulse, which bears same results as the ones obtained from the semi-classical description. This exercise helps to have an in-depth understanding of the process. Finally, we provide a geometric representation of the detection process on the Majorana sphere. We begin by presenting detailed analysis of interaction-free measurements in general and its coherent counterpart.

SUPPLEMENTARY NOTE 1: FIGURES OF MERIT

The Positive Ratio $PR = p_0(\theta)/(p_0(\theta) + p_1(\theta))$ is the measure of correct detection of B-pulse with arbitrary strength (θ) and the Negative Ratio $NR = p_1(\theta)/(p_0(\theta) + p_1(\theta))$ is the incorrect non-detection of the B-pulse when it is applied with strength (θ). Special cases are defined as follows: FPR and TNR correspond to $\theta = 0$, while TPR and FNR correspond to $\theta = \pi$ for PR and NR respectively. In fact, $PR(\theta)$ effectively corresponds to the number of instances that report an interaction-free measurement of the B-pulse and $NR(\theta)$ are the inconclusive outcomes, where both of these quantities are obtained by excluding the situations where B-pulses are absorbed (or the bomb is exploded). This means that for $N = 1$, $\theta = \pi$, and most importantly- the case when B-pulse is not absorbed, there is 50% chance that the presence of B-pulse will be confirmed: interaction-free detection of the B-pulse and remaining 50% of the times, we are not sure whether B-pulse is present or not, *i.e.* an inconclusive outcome. The extension of this logic for the case of large N suggests that larger values of $PR(\theta)$ have direct correspondence with

increasing probability of interaction-free/absorption-free detection of the B-pulse of strength θ . In analogy with the optical case [4, 5], we can also introduce the coherent interaction-free efficiency $\eta_c(\theta) = p_0(\theta)/[p_0(\theta) + p_2(\theta)]$ as the fraction of pulses detected in an interaction-free manner while discarding the inconclusive results.

It is also important to emphasize the role of setting the Ramsey sequence such as, in the absence of the pulse, the final state is $|1\rangle$ and not say some superposition of $|0\rangle$ and $|1\rangle$. This ensures that, when finding the system in the state $|0\rangle$, we know with 100% certainty that the pulse was present, in other words that $FPR=0$ and $TNR=1$ in the ideal case.

SUPPLEMENTARY NOTE 2: COHERENT VERSUS PROJECTIVE INTERACTION-FREE MEASUREMENTS

We discuss here the difference between the standard non-unitary (projective) interaction-free measurement and our approach. To make the connection clear, we start with the $N = 1$ case, for which simple analytical results can be provided.

$N = 1$ case

From the definitions in the main text we have

$$S_1 = \frac{1}{\sqrt{2}}\mathbb{I}_{01} - \frac{i}{\sqrt{2}}\sigma_{01}^y + |2\rangle\langle 2|, \quad (6)$$

$$B(\theta) = |0\rangle\langle 0| + \cos\frac{\theta}{2}\mathbb{I}_{12} - i\sin\frac{\theta}{2}\sigma_{12}^y, \quad (7)$$

where $\mathbb{I}_{kl} = |k\rangle\langle k| + |l\rangle\langle l|$ and $\sigma_{kl}^y = -i|k\rangle\langle l| + i|l\rangle\langle k|$.

The corresponding Mach-Zehnder interferometric setup for non-unitary interaction-free measurements is shown in Fig. 8. This corresponds to a “bomb”, which is non-ideal in the sense that the probability of “explosion” in the presence of a single photon is not necessarily unity. This situation is modeled by the insertion of a beam splitter with finite reflectivity.

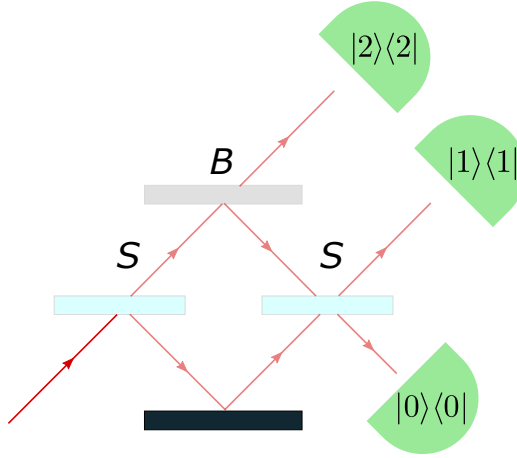


FIG. 8. Standard interaction-free interferometric setup, where the absorption probability is in general not unity.

To analyze what happens, let us first notice that in the absence of the B-pulse there is obviously no difference between the two approaches – in both cases the evolution operator is the unitary $S_1^2 = -i\sigma_{01}^y + |2\rangle\langle 2|$. But, in the presence of a B-pulse, the superposition created by S_1 gets modified to

$$B(\theta)S_1|0\rangle = \frac{1}{\sqrt{2}}|0\rangle + \frac{1}{\sqrt{2}}\cos\frac{\theta}{2}|1\rangle + \frac{1}{\sqrt{2}}\sin\frac{\theta}{2}|2\rangle. \quad (8)$$

The measurement operators associated with the detector $|2\rangle\langle 2|$ clicking (absorption) or not clicking (non-absorption) are the projectors

$$P_{\text{abs}} = |2\rangle\langle 2|, \quad (9)$$

$$P_{\text{abs}} = |0\rangle\langle 0| + |1\rangle\langle 1|. \quad (10)$$

Thus, with probability $p_{\text{abs}}(\theta) = \langle 0|S_1^\dagger B^\dagger(\theta)P_{\text{abs}}B(\theta)S_1|0\rangle = (1/2)\sin^2(\theta/2)$ the state of the system collapses to $(1/\sqrt{p_{\text{abs}}(\theta)})P_{\text{abs}}B(\theta)S_1|0\rangle = |2\rangle$ if a click is recorded by the detector $|2\rangle\langle 2|$; otherwise, with probability $p_{\text{abs}}(\theta) = \langle 0|S_1^\dagger B^\dagger(\theta)P_{\text{abs}}B(\theta)S_1|0\rangle = 1/2 + (1/2)\cos^2(\theta/2)$, the state collapses onto $(1/\sqrt{p_{\text{abs}}(\theta)})P_{\text{abs}}B(\theta)S_1|0\rangle = (1/\sqrt{1+\cos(\theta/2)})(|0\rangle + \cos(\theta/2)|1\rangle)$. Therefore, a non-absorption event has consequences: it confines the state to the $\{|0\rangle, |1\rangle\}$ manifold. For the case $\theta = \pi$, this confinement is onto the state $|0\rangle$ (we know for sure that the photon has traveled only in one branch on the interferometer), while the case $\theta = 0$ corresponds to a completely reflective beam-splitter B, which fully hides the detector $|2\rangle\langle 2|$, and as a result the equal-weight superposition of $|0\rangle$ and $|1\rangle$ is not affected.

Note here that we can define the POVM measurement operators associated with the ensemble B-splitter plus $|2\rangle\langle 2|$ -detector by $M_{\text{abs}} = P_{\text{abs}}B$ and $M_{\text{abs}} = P_{\text{abs}}B$, with the property $M_{\text{abs}}^\dagger M_{\text{abs}} + M_{\text{abs}}^\dagger M_{\text{abs}} = \mathbb{I}_3$, where \mathbb{I}_3 is the 3×3 identity matrix.

The density matrix after the second beam splitter can be found by applying again S_1 to the states written above. Therefore, the state at the output is

$$\left(\sin^2\frac{\theta}{4}|0\rangle + \cos^2\frac{\theta}{4}|1\rangle\right)\left(\sin^2\frac{\theta}{4}|0\rangle + \cos^2\frac{\theta}{4}|1\rangle\right) + \frac{1}{2}\sin^2\frac{\theta}{2}|2\rangle\langle 2|. \quad (11)$$

As a result, the probability of interaction-free detection is $p_{\text{det}} = \sin^4(\theta/4)$ (detector $|0\rangle\langle 0|$ clicks) and the efficiency η , defined as the fraction of successful detections by excluding the inconclusive cases ($|1\rangle\langle 1|$ clicks) is

$$\eta = \frac{p_{\text{det}}}{p_{\text{det}} + p_{\text{abs}}} = \frac{2\sin^4(\theta/4)}{2\sin^4(\theta/4) + \sin^2(\theta/2)}. \quad (12)$$

Consider now the coherent case. At the end of the protocol, the state is

$$S_1 B(\theta) S_1 |0\rangle = \sin^2\frac{\theta}{4}|0\rangle + \cos^2\frac{\theta}{4}|1\rangle + \frac{1}{\sqrt{2}}\sin\frac{\theta}{2}|2\rangle. \quad (13)$$

We can immediately verify that, by applying the same projectors P_{abs} and P_{abs} corresponding to a measurement of the state $|2\rangle$, we obtain precisely the result Eq. (11). We have $p_0 = \sin^4(\theta/4)$, $p_1 = \cos^4(\theta/4)$, $p_2 = (1/2)\sin^2(\theta/2)$ and the coherent-case efficiency is

$$\eta_c = \frac{p_0}{p_0 + p_2} = \frac{2\sin^4(\theta/4)}{2\sin^4(\theta/4) + \sin^2(\theta/2)}, \quad (14)$$

the same as Eq. (12). This is due to the fact that $S_1 P_{\text{abs}} = P_{\text{abs}} S_1$ and $S_1 P_{\text{abs}} = P_{\text{abs}} S_1$, so it does not matter when we record the result of the projection on $|2\rangle\langle 2|$.

In conclusion, for $N = 1$ there is no difference in success/failure probabilities and efficiency between the coherent and projective case. The corresponding experimental results are shown in Fig. 9, together with a comparison with the simulations and with the ideal (decoherence-free) case.

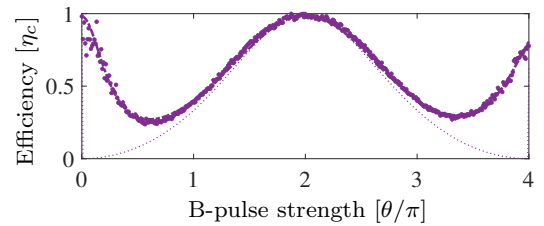


FIG. 9. Corresponding to each B-pulse strength, the coherent efficiency $\eta_c(\theta) = p_0(\theta)/(p_0(\theta) + p_2(\theta))$ obtained from the experiment is shown as a purple line with circular markers, closely followed by the simulated curve (purple dot-dashed). The thin dotted purple line represents the respective ideal case, with no decoherence and without any experimental imperfections.

Quantizing the B-pulse in the $N = 1$ case

We can get a deeper understanding of this effect by looking at the case where we treat the B-pulse quantum

mechanically rather than in the semiclassical approximation. Let us denote by b and b^\dagger the annihilation and creation operator describing the presence of photons from the B-pulse. In the rotating wave approximation, the interaction Hamiltonian between the pulse and the transmon is

$$H_{\text{int}} = \frac{i\hbar g}{2} (b^\dagger |1\rangle\langle 2| - b |2\rangle\langle 1|). \quad (15)$$

Consider now a Fock state $|n\rangle$ with n photons. Experimentally, this can be realized as a cavity or resonator to which the transmon can be coupled and uncoupled. In the subspace spanned by the vectors $|n\rangle\otimes|1\rangle$ and $|n-1\rangle\otimes|2\rangle$ this Hamiltonian can be diagonalized. The eigenvectors are

$$|n+\rangle = \frac{1}{\sqrt{2}} (|n\rangle\otimes|1\rangle - i|n-1\rangle\otimes|2\rangle), \quad (16)$$

$$|n-\rangle = \frac{-1}{\sqrt{2}} (|n\rangle\otimes|1\rangle + i|n-1\rangle\otimes|2\rangle), \quad (17)$$

and the eigenvalues are $E_{\pm} = \pm(\hbar/2)g\sqrt{n}$, corresponding to a Rabi frequency $g\sqrt{n}$. Assume now a certain duration of the B-pulse – let's denote it τ_B . We can define the corresponding strength θ_n of the n -photon pulse as $\theta_n = g\sqrt{n}\tau_B$. We start in the state $|n\rangle\otimes|0\rangle$ and apply S_1 , B (via the interaction Hamiltonian Eq. 15), and again S_1 . The final result is the state

$$\sin^2 \frac{\theta_n}{4} |n\rangle\otimes|0\rangle + \cos^2 \frac{\theta_n}{4} |n\rangle\otimes|1\rangle + \frac{1}{\sqrt{2}} \sin \frac{\theta_n}{2} |n-1\rangle\otimes|2\rangle. \quad (18)$$

First, we can immediately compare this result with the semiclassical expression Eq. (13), to check that the probabilities are the same. But most importantly, Eq. (18) shows the entanglement and the energy balance between the pulse and the detector: if the transmon is found in the state $|0\rangle$ then the pulse will still contain n photons - no photon has been absorbed. On the contrary, if the transmon is found in state $|2\rangle$, this could happen only with the absorption of a photon from the B-pulse.

$N = 2$ case

For the $N = 2$ case the beam splitter S_2 is a $\pi/3$ pulse

$$S_2 = \frac{\sqrt{3}}{2} \mathbb{I}_{01} - \frac{i}{2} \sigma_{01}^y + |2\rangle\langle 2|. \quad (19)$$

The final state is

$$\begin{aligned} \frac{1}{8} & \left[3\sqrt{3} - \sqrt{3} \cos \frac{\theta_1}{2} - 2\sqrt{3} \cos^2 \frac{\theta_1}{4} \cos \frac{\theta_2}{2} \right. \\ & + 2 \sin \frac{\theta_1}{2} \sin \frac{\theta_2}{2} \left. \right] |0\rangle + \frac{1}{8} \left[3 - \cos \frac{\theta_1}{2} \right. \\ & + 6 \cos^2 \frac{\theta_1}{4} \cos \frac{\theta_2}{2} - 2\sqrt{3} \sin \frac{\theta_1}{2} \sin \frac{\theta_2}{2} \left. \right] |1\rangle \\ & + \frac{1}{2} \left[\sin \frac{\theta_1}{2} \cos \frac{\theta_2}{2} + \sqrt{3} \cos^2 \frac{\theta_1}{4} \sin \frac{\theta_2}{2} \right] |2\rangle. \end{aligned} \quad (20)$$

At maximum strength $\theta_1 = \theta_2 = \pi$ this state reads

$$\frac{1}{8} (2 + 3\sqrt{3}) |0\rangle + \frac{1}{8} (3 - 2\sqrt{3}) |1\rangle + \frac{1}{4} \sqrt{3} |2\rangle. \quad (21)$$

We can already see that the probability of absorption is $p_2 = 3/16 = 0.1875$, smaller than the 0.25 of the single-interrogation detection and the probability of an IFM detection (ground-state population) is $p_0 = (31 + 12\sqrt{3})/64 \approx 0.8091$, significantly larger than the 0.25 of the single-interrogation case. The efficiency of the coherent detection is

$$\eta_c = \frac{p_0}{p_0 + p_2} = 0.8118. \quad (22)$$

Note that the efficiency is so high because the probability of failing to find the pulse is very small, $p_1 = 0.0034$.

Further, we experimentally realize a general case where B-pulse strengths are different, *i.e.* $\theta_1, \theta_2 \in [0, 4\pi]$. Experimental and simulated results for the efficiency η_c is shown as a map as functions of θ_1 and θ_2 in Fig. 10. Variation of the ground state, first excited state and second excited state populations as functions of θ_1 and θ_2 are shown in the main text alongwith the Positive Ratio $PR(\theta_1, \theta_2) = p_0(\theta_1, \theta_2)/(p_0(\theta_1, \theta_2) + p_1(\theta_1, \theta_2))$ and the Negative Ratio $NR(\theta_1, \theta_2) = p_1(\theta_1, \theta_2)/(p_0(\theta_1, \theta_2) + p_1(\theta_1, \theta_2))$. Experimental and simulated results are in very good agreement with each other.

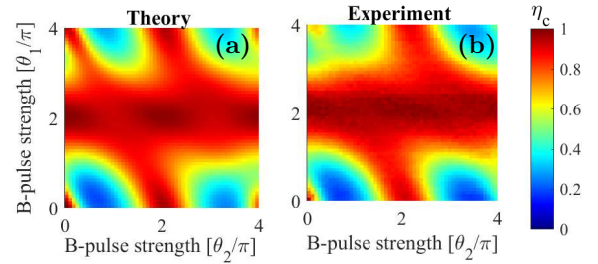


FIG. 10. Simulated and experimental map of coherent efficiency η_c as a function of θ_1 and θ_2 .

Importantly, we also observe that the previous maximum at $\theta = 2\pi$ from the $N = 1$ case (see Fig. 2 in the main text) starts to flatten, evolving towards becoming a plateau, a tendency that will become even more prominent for $N \gg 1$.

Let us now clarify the difference with respect to the standard projective (non-unitary) interaction-free measurement, considering for simplicity the case $\theta_1 = \theta_2 = \pi$. After the first pulse of strength θ_1 the state becomes

$$B(\theta_1)S_2|0\rangle = \frac{\sqrt{3}}{2} |0\rangle + \frac{1}{2} \cos \frac{\theta_1}{2} |1\rangle + \frac{1}{2} \sin \frac{\theta_1}{2} |2\rangle. \quad (23)$$

This is the state that serves as the input for the next Ramsey S_2 pulse.

We can now see that there is a crucial difference with respect to the case when there has been a measurement

of the second excited state and the result was negative. In this situation, the state entering the second S_2 pulse is

$$\begin{aligned} & \frac{1}{\sqrt{p_{\text{abs}}(\theta_1)}} P_{\text{abs}} B(\theta_1) S_2 |0\rangle = \\ & = \frac{1}{\sqrt{3 + \cos^2(\theta_1/2)}} \left(\sqrt{3} |0\rangle + \cos \frac{\theta_1}{2} |1\rangle \right) \end{aligned} \quad (24)$$

where $p_{\text{abs}}(\theta_1) = \frac{3}{4} + \frac{1}{4} \cos^2(\theta_1/2)$. Unlike Eq. (23), this state does not have a component on $|2\rangle$. In the case $\theta_1 = \pi$, the state Eq. (24) seen by the second S_2 pulse is $|0\rangle$, the same as the initial one. Thus, the same interference phenomena is reproduced in the second Ramsey cycle. In contrast, the coherent-case Eq. (23) contains a component on $|2\rangle$, which precisely encapsulates our lack of knowledge about the population on state $|2\rangle$ at the beginning of the second Ramsey cycle.

We can also calculate the probabilities and efficiency in the non-unitary case for $\theta_1 = \theta_2 = \pi$, $p_{\text{det}} = (\cos^2(\pi/6))^3 = 27/64 = 0.4219$ and $p_{\text{abs}} = \sin^2(\pi/6)[1 + \cos^2(\pi/6)] = 7/16 = 0.4375$ resulting in an efficiency

$$\eta = \frac{p_{\text{det}}}{p_{\text{det}} + p_{\text{abs}}} = 0.49. \quad (25)$$

We can see that in the $N = 2$ case the efficiency in the coherent case is significantly larger!

Quantizing the B-pulse in the $N = 2$ case

In a way similar to the $N = 1$ case, we can treat the B-pulse quantum mechanically. We consider that an interaction Hamiltonian Eq. (15) is available, such that the transmon can be coupled in a controllable way to the field.

Suppose that the transmon is coupled in both sequences to the same mode containing n photons. These photons can be for example located in a cavity, which is coupled by a tunable coupling element to the transmon, or they can be traveling in a transmission line, as in our experiments. The initial state is $|n\rangle \otimes |0\rangle$. The final state can be obtained by the same procedure as in the $N = 1$ case, and reads

$$\begin{aligned} & \frac{1}{8} \left[3\sqrt{3} - \sqrt{3} \cos \frac{\theta_{1n}}{2} - 2\sqrt{3} \cos^2 \frac{\theta_{1n}}{4} \cos \frac{\theta_{2n}}{2} + \right. \\ & \left. + 2 \sin \frac{\theta_{1n}}{2} \sin \frac{\theta_{2n}}{2} \right] |n\rangle \otimes |0\rangle + \\ & \frac{1}{8} \left[3 - \cos \frac{\theta_{1n}}{2} + 6 \cos^2 \frac{\theta_{1n}}{4} \cos \frac{\theta_{2n}}{2} \right. \\ & \left. - 2\sqrt{3} \sin \frac{\theta_{1n}}{2} \sin \frac{\theta_{2n}}{2} \right] |n\rangle \otimes |1\rangle + \\ & + \frac{1}{2} \left[\sin \frac{\theta_{1n}}{2} \cos \frac{\theta_{2n}}{2} + \sqrt{3} \cos^2 \frac{\theta_{1n}}{4} \sin \frac{\theta_{2n}}{2} \right] |n-1\rangle \otimes |2\rangle \end{aligned} \quad (26)$$

with the notation $\theta_{1n} = g_1 \sqrt{n} t_{B1}$ and $\theta_{2n} = g_2 \sqrt{n} t_{B2}$. We observe immediately the similarity with the semiclassical

result Eq. (20). The result puts very clearly in evidence again that, by finding the qubit in the state $|0\rangle$ the photonic Fock state does not change. It can lose a photon only if the level $|2\rangle$ is excited. Thus, we can detect the existence of photons inside the cavity without absorbing any of them.

Generalization to two different modes: We can imagine also the situation when the transmon is coupled to different modes in the two sequences, for example realized as photons in two distinct cavities. Suppose that in the first sequence it interacts with a cavity containing n photons, while in the second sequence it interacts with another cavity, containing m photons. The initial state is then $|m, n\rangle \otimes |0\rangle$. The final state in this case can be calculated as

$$\begin{aligned} & \frac{1}{8} \left[\left(3\sqrt{3} - \sqrt{3} \cos \frac{\theta_{1n}}{2} - 2\sqrt{3} \cos^2 \frac{\theta_{1n}}{4} \cos \frac{\theta_{2m}}{2} \right) |m, n\rangle \right. \\ & \left. + 2 \sin \frac{\theta_{1n}}{2} \sin \frac{\theta_{2m+1}}{2} |m+1, n-1\rangle \right] \otimes |0\rangle + \\ & \frac{1}{8} \left[\left(3 - \cos \frac{\theta_{1n}}{2} + 6 \cos^2 \frac{\theta_{1n}}{4} \cos \frac{\theta_{2m}}{2} \right) |m, n\rangle \right. \\ & \left. - 2\sqrt{3} \sin \frac{\theta_{1n}}{2} \sin \frac{\theta_{2m+1}}{2} |m+1, n-1\rangle \right] \otimes |1\rangle + \\ & + \frac{1}{2} \left[\sin \frac{\theta_{1n}}{2} \cos \frac{\theta_{2m+1}}{2} |m, n-1\rangle + \right. \\ & \left. \sqrt{3} \cos^2 \frac{\theta_{1n}}{4} \sin \frac{\theta_{2m}}{2} |m-1, n\rangle \right] \otimes |2\rangle, \end{aligned} \quad (27)$$

with the notation $\theta_{1n} = g_1 \sqrt{n} t_{B1}$ and $\theta_{2m} = g_2 \sqrt{m} t_{B2}$, $\theta_{2m+1} = g_2 \sqrt{m+1} t_{B2}$. If the transmon gets excited, we see that this can happen with the loss of a photon from either one of the modes. If the transmon is found in the state $|0\rangle$, then we can ascertain the existence of photons in the cavities, and, at the same time, we have transformed the initial Fock state $|m, n\rangle$ into a coherent superposition of $|m, n\rangle$ and $|m+1, n-1\rangle$. The latter of course represents the possibility that a photon gets absorbed by the transmon during the first Ramsey sequence and reemitted into the same cavity during the second sequence. The transformation of a Fock state into a coherent state is a feature that is reminiscent of the famous Hanbury-Brown and Twiss experiment.

$N > 1$ case

We have seen that for $N = 1$ the efficiency of the coherent protocol is the same as that of the projective protocol, while for $N = 2$ the coherent protocol is more advantageous. Does this tendency continues for large N ? Let us take one more step and look at the case $N = 3$. In the

coherent protocol, the output state is

$$\begin{aligned} & \cos \frac{\pi}{8} \left(\cos^3 \frac{\pi}{8} + 2 \sin^2 \frac{\pi}{8} \right) |0\rangle \\ & + \sin \frac{\pi}{8} \left(\cos^3 \frac{\pi}{8} + \sin^2 \frac{\pi}{8} - \cos^2 \frac{\pi}{8} \right) |1\rangle \\ & + \sin \frac{\pi}{8} \cos \frac{\pi}{8} \left(\cos \frac{\pi}{8} - 1 \right) |2\rangle. \end{aligned} \quad (28)$$

We can verify immediately that $p_0 > \cos^8(\pi/8) = p_{\text{det}}$ and $p_2 < \sin^2(\pi/8)(1 + \cos^2(\pi/8) + \cos^4(\pi/8)) = p_{\text{abs}}$, where p_{det} and p_{abs} are the detection and absorption probabilities in the $N = 3$ case, respectively.

We can now generalize the protocol to N B-pulses and the same number of Ramsey sequences. In this case the S pulses are defined as

$$S_N = \exp \left[-i \frac{\pi}{2(N+1)} \sigma_{01}^y \right] \quad (29)$$

The efficiency of the coherent detection is defined as before.

$$\eta_c = \frac{p_0}{p_0 + p_2}. \quad (30)$$

Let us consider now the non-unitary (projective) protocol. In this case the probability of a successful detection is the product of probabilities that the system stays in the state $|0\rangle$

$$p_{\text{det}} = \left[\cos \left(\frac{\pi}{2(N+1)} \right) \right]^{2(N+1)}, \quad (31)$$

while the absorption probability is

$$p_{\text{abs}} = \sin^2 \left(\frac{\pi}{2(N+1)} \right) \sum_{n=0}^{N-1} \left[\cos \left(\frac{\pi}{2(N+1)} \right) \right]^{2n}. \quad (32)$$

The second expression is a sum of independent probabilities (that there is absorption in the first Ramsey sequence, that there is no absorption in the first Ramsey sequence but there is in the second, etc.). The efficiency is

$$\eta = \frac{p_{\text{det}}}{p_{\text{det}} + p_{\text{abs}}}. \quad (33)$$

The efficiencies obtained in the coherent and the projective cases for $N \in [1, 25]$ are plotted in Fig. 11, with and without decoherence. Clearly, the efficiency obtained in the coherent case is significantly higher than that of the projective case, *i.e.* $\eta_c > \eta$ and $\eta_c^{(d)} > \eta^{(d)}$. In the presence of decoherence, the difference between the two cases tends to stay constant with increasing N .

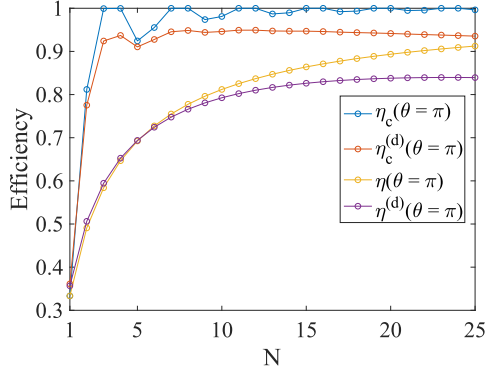


FIG. 11. The efficiency of our scheme η_c as a function of N Ramsey segments is compared with the efficiency of the standard projective scheme η , all at strength $\theta = \pi$. The corresponding cases with dissipation included are denoted by $\eta_c^{(d)}$ and $\eta^{(d)}$.

Elements of the confusion matrix in coherently repeated interrogations. We can obtain the elements of the con-

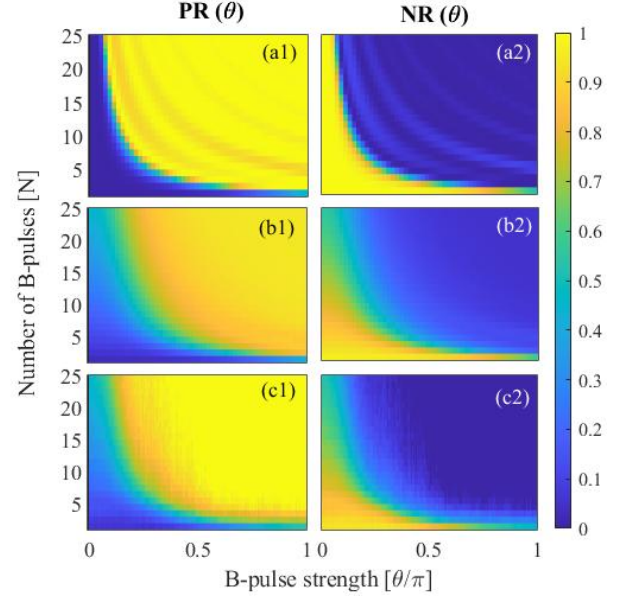


FIG. 12. (a1, b1, c1) Positive ratio, $\text{PR}(\theta)$ and (a2, b2, c2) Negative ratio, $\text{NR}(\theta)$ are plotted for different number of B-pulses N with equal strengths θ , where $\theta \in [0, \pi]$ linearly sweeps the range of B-pulse strengths for a given $N \in [1, 25]$. Panels (a1,a2) present the ideal situation with no decoherence, panels (b1,b2) are the results obtained from simulation with decoherence and panels (c1,c2) correspond to the results from the experiments.

fusion matrix in a more general form for the case of N B-pulses, see Fig. (12). The general 2D maps of these positive and negative ratios are plotted as functions of number of B-pulses and B-pulse strength as shown in Fig. (12) for ideal simulation without decoherence, simulation with decoherence, and results from the experiments. It is clear from the surface maps in Fig. (12) that the True Positive Ratio (TPR) is close to 1 and the False Negative Ratio

(FNR) is close to 0 for $N > 2$ as observed from the simulated and the experimental results. Ideally, FPR and TNR are independent of N , but there is increase in FPR values and decrease in TNR values with increasing N in parts (b1,b2,c1,c2) of Fig. (12), which is due to the long sequences, where decoherence is significant.

Next, let us reconsider the p_0 profiles for various different values of N as a function of θ , where for a given N , all the B-pulses are of the same strength θ , varying linearly between $[0, \pi]$ as shown in Fig. 4(a) of the main text. As expected, p_0 gradually rises from 0 to a maximum value with increasing θ and then tends to stay higher, forming a plateau which is symmetrical around $\theta = 2\pi$. This plateau gets wider with increasing N . We quantify the widening in terms of the area $\int_0^\pi d\theta p_0(\theta)$ enclosed under p_0 – as a function of θ – for a given N and for $\theta \in [0, \pi]$. The results for equal and unequal arbitrary B-pulse strengths are shown in Fig. 13 (a,b) respectively. Evaluation of area from the experimental data is shown with red square markers, with the simulation as continuous black curve. The dotted black curve is the simulation without considering the depolarization channel, while the dashed black curve stands for the ideal case without decoherence. As expected, the simulation in the absence of depolarization predicts higher values than without depolarization, while the ideal case provides the upper limit to the area. Note also that the respective plots of area for unequal B-pulse strengths are higher than for equal B-pulse strengths. This, one more time, conveys the idea that unequal random B-pulse strengths give rise to higher efficiency of coherent interaction-free detection.

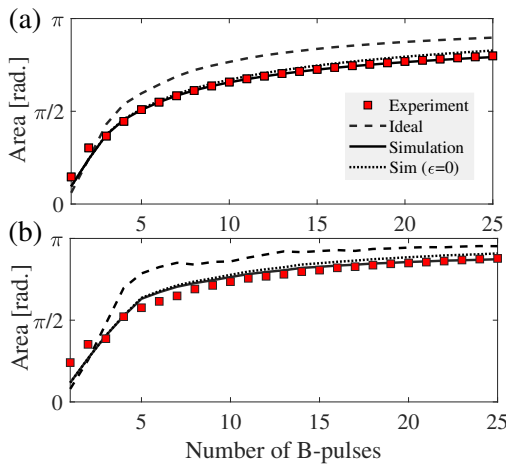


FIG. 13. Area under the $p_0(\theta)$ plots as a function of N with $\theta \in [0, \pi]$ for (a) Identical B-pulses with linearly varying strengths, (b) Randomly chosen B-pulses.

Quantizing the B-pulse in the $N > 1$ case

Similarly to $N = 2$, if we interrogate a single mode with n photons, the 3×3 matrix structure of the semiclassical case will be preserved with the replacement $|0\rangle \rightarrow |n\rangle \otimes |0\rangle$, $|1\rangle \rightarrow |n\rangle \otimes |1\rangle$, and $|2\rangle \rightarrow |n\rangle \otimes |2\rangle$, as it is clear from the $N = 2$ case already. Thus, all the results obtained in this paper can be applied to this situation as well.

Generalization to multiple modes A different scenario can be envisioned if several different modes are available, when clearly a variety of options exist on how to interrogate them. In this case, states that correspond to superpositions of these modes will be obtained when the transmon is found in the ground state, similarly to what has been observed already for $N = 2$. Thus, our protocol can be generalized to simultaneous detection of photons in several cavities.

SUPPLEMENTARY NOTE 3: GENERAL RESULTS FOR $N \geq 1$ COHERENT INTERACTION-FREE DETECTION

A number of theoretical results for the case of $N \geq 1$ are presented in this section.

General analytical results

For the coherent case, the subsequent evolution for a system of size N is just $(SB)^N S|0\rangle$. Let us denote the wavefunction after the j^{th} Ramsey segment as $|\psi\rangle_j = \alpha_j|0\rangle + \beta_j|1\rangle + \gamma_j|2\rangle$. The probability amplitudes $\alpha_j, \beta_j, \gamma_j$ obey the recursion relations

$$\alpha_{j+1} = \cos \frac{\pi}{2(N+1)} \alpha_j \quad (34)$$

$$- \sin \frac{\pi}{2(N+1)} \cos \frac{\theta_{j+1}}{2} \beta_j + \sin \frac{\pi}{2(N+1)} \sin \frac{\theta_{j+1}}{2} \gamma_j,$$

$$\beta_{j+1} = \sin \frac{\pi}{2(N+1)} \alpha_j \quad (35)$$

$$+ \cos \frac{\pi}{2(N+1)} \cos \frac{\theta_{j+1}}{2} \beta_j - \cos \frac{\pi}{2(N+1)} \sin \frac{\theta_{j+1}}{2} \gamma_j,$$

$$\gamma_{j+1} = \sin \frac{\theta_{j+1}}{2} \beta_j + \cos \frac{\theta_{j+1}}{2} \gamma_j. \quad (36)$$

In the case of identical pulses $\theta_j = \theta$, starting with the probability amplitudes Eqs. (35, 36, 36), we observe that these recursion relations yield sums of even functions of θ (cosines) α_j and β_j , and sums of odd functions of θ (sines) γ_j . Specifically, the amplitudes in the coherent case can

be expressed as the expansions

$$\alpha_j = \sum_{k=0}^j C_j[k] \cos \frac{k\theta}{2}, \quad (37)$$

$$\beta_j = \sum_{k=0}^j C'_j[k] \cos \frac{k\theta}{2}, \quad (38)$$

$$\gamma_j = \sum_{k=0}^j C''_j[k] \sin \frac{k\theta}{2}. \quad (39)$$

From the recursion relations Eqs. (35, 36, 36), we find the following relations among the coefficients

$$C_{j+1}[k] = \cos \frac{\pi}{2(N+1)} C_j[k]_{k=0,j} \quad (40)$$

$$- \frac{1}{2} \sin \frac{\pi}{2(N+1)} [C'_j[k+1] - C''_j[k+1]]_{k=-1,j-1}$$

$$- \frac{1}{2} \sin \frac{\pi}{2(N+1)} [C'_j[k-1] + C''_j[k-1]]_{k=1,j+1}$$

$$C'_{j+1}[k] = \sin \frac{\pi}{2(N+1)} C_j[k]_{k=0,j} \quad (41)$$

$$+ \frac{1}{2} \cos \frac{\pi}{2(N+1)} [C'_j[k+1] - C''_j[k+1]]_{k=-1,j-1}$$

$$+ \frac{1}{2} \cos \frac{\pi}{2(N+1)} [C'_j[k-1] + C''_j[k-1]]_{k=1,j+1}$$

$$C''_{j+1}[k] = \frac{1}{2} [C'_j[k-1] + C''_j[k-1]]_{k=1,j+1} \quad (42)$$

$$- \frac{1}{2} [C'_j[k+1] - C''_j[k+1]]_{k=-1,j}$$

Here we use the notation $[\dots]_{k=\dots}$ to denote a restriction over the values of k . The final probabilities can be then easily calculated as $p_0 = \alpha_N^2$, $p_1 = \beta_N^2$, and $p_2 = \gamma_N^2$. The coefficients for systems of sizes $N = 1$, $N = 2$, $N = 3$, and $N = 4$ are shown in Tabs. I-III.

	$\mathbf{N = 1}$	$\mathbf{N = 2}$	$\mathbf{N = 3}$	$\mathbf{N = 4}$
$\mathbf{C_N[0]}$	0.5	0.67	0.75	0.80
$\mathbf{C_N[1]}$	-0.5	-0.43	-0.36	-0.31
$\mathbf{C_N[2]}$	0	-0.23	-0.25	-0.24
$\mathbf{C_N[3]}$	0	0	-0.14	-0.16
$\mathbf{C_N[4]}$	0	0	0	-0.089

TABLE I. The probability amplitude coefficients for p_0 (coherent case) up to two significant digits with sequences of length $N = 1$, $N = 2$, $N = 3$, and $N = 4$.

	$\mathbf{N = 1}$	$\mathbf{N = 2}$	$\mathbf{N = 3}$	$\mathbf{N = 4}$
$\mathbf{C'_N[0]}$	0.5	0.35	0.27	0.22
$\mathbf{C'_N[1]}$	0.5	0.25	0.17	0.13
$\mathbf{C'_N[2]}$	0	0.40	0.23	0.17
$\mathbf{C'_N[3]}$	0	0	0.33	0.21
$\mathbf{C'_N[4]}$	0	0	0	0.27

TABLE II. The probability amplitude coefficients for p_1 (coherent case) up to two significant digits with sequences of length $N = 1$, $N = 2$, $N = 3$, and $N = 4$.

	$\mathbf{N = 1}$	$\mathbf{N = 2}$	$\mathbf{N = 3}$	$\mathbf{N = 4}$
$\mathbf{C''_N[1]}$	0.71	0.43	0.33	0.27
$\mathbf{C''_N[2]}$	0	0.47	0.31	0.24
$\mathbf{C''_N[3]}$	0	0	0.35	0.25
$\mathbf{C''_N[4]}$	0	0	0	0.29

TABLE III. The probability amplitude coefficients for p_2 (coherent case) up to two significant digits with sequences of length $N = 1$, $N = 2$, $N = 3$, and $N = 4$.

The recurrence relations allow us to get a deeper understanding of the process of coherent accumulation of amplitude probabilities in successive pulses. Let us consider the maximum-strength pulses $\theta_j = \pi$, for which the relations Eqs. (35, 36, 36) become

$$\alpha_{j+1} = \cos \frac{\pi}{2(N+1)} \alpha_j + \sin \frac{\pi}{2(N+1)} \gamma_j, \quad (43)$$

$$\beta_{j+1} = \sin \frac{\pi}{2(N+1)} \alpha_j - \cos \frac{\pi}{2(N+1)} \gamma_j, \quad (44)$$

$$\gamma_{j+1} = \beta_j. \quad (45)$$

We notice that if the dominant probability amplitude is the one corresponding to the ground state, this relationship tends to be preserved under successive application of the sequences. Indeed, from Eq. (45) we see that if β_j is small, then γ_{j+1} will be small as well. From Eq. (44) we see that the relatively large probability amplitude α_j gets multiplied by a small number $\sin \frac{\pi}{2(N+1)}$, and the remaining part of the equation contains also the relatively small γ_j . To make this observation more precise, we note that the general form of the probability amplitudes is

$$\alpha_j = \cos^{j+1} \frac{\pi}{2(N+1)} + \sin^2 \frac{\pi}{2(N+1)} \mathcal{P}_{\alpha_j}^{(j-2)} \left(\cos \frac{\pi}{2(N+1)} \right),$$

$$\beta_j = \sin \frac{\pi}{2(N+1)} \mathcal{P}_{\beta_j}^{(j)} \left(\cos \frac{\pi}{2(N+1)} \right),$$

$$\gamma_j = \sin \frac{\pi}{2(N+1)} \mathcal{P}_{\gamma_j}^{(j-1)} \left(\cos \frac{\pi}{2(N+1)} \right).$$

where $\mathcal{P}^{(j)}$ are j -order polynomials in the variable $\xi = \cos \frac{\pi}{2(N+1)}$ satisfying

$$\begin{aligned}\mathcal{P}_{\alpha_{j+1}}^{(j-1)}(\xi) &= \xi \mathcal{P}_{\alpha_j}^{(j-2)}(\xi) + \mathcal{P}_{\gamma_j}^{(j-1)}(\xi), \\ \mathcal{P}_{\beta_{j+1}}^{(j+1)}(\xi) &= \xi^{j+1} - \xi^2 \mathcal{P}_{\alpha_j}^{(j-2)}(\xi) - \xi \mathcal{P}_{\gamma_j}^{(j-1)}(\xi) + \mathcal{P}_{\alpha_j}^{(j-2)}(\xi), \\ \mathcal{P}_{\gamma_{j+1}}^{(j)}(\xi) &= \mathcal{P}_{\beta_j}^{(j)}(\xi).\end{aligned}$$

We can see that the coefficients β_j and γ_j get multiplied by the small quantity $\sin \frac{\pi}{2(N+1)}$ at every iteration, therefore they tend to decrease. On the contrary, α_j accumulates the relatively larger quantity $\cos^{j+1} \frac{\pi}{2(N+1)}$, with $\lim_{N \rightarrow \infty} \cos^{N+1} \frac{\pi}{2(N+1)} = 1$. Thus, at the end of the protocol, we will have $p_0 = |\alpha_{N+1}|^2 = \cos^{2(N+1)} \frac{\pi}{2(N+1)} + \sin^2 \frac{\pi}{2(N+1)}$. The first term equals the projective probability, see Eq. (31), while the rest of terms are the result of coherent accumulation of amplitude probabilities during the sequences. We therefore expect a higher p_0 in the coherent case, and therefore a lower probability of absorption p_2 . This is calculated also numerically in the next subsection.

Numerical results: cumulative probability of absorption

We have seen that the projective case of interaction-free detection completely excludes the situations where a B-pulse is absorbed by collapsing the wavefunction onto the state $|0\rangle$, which does not interact with the pulse. On the other hand, the coherent-interrogation interaction-free measurement protocol yields detection with very high probability, which is demonstrated by simulations as well as by experiments. We can introduce a figure of merit that allows us to quantify in a single number the probabilities of B-pulse absorption at different sequences. We can quantify this concisely by keeping track of the probability of absorption instances with $\theta = \pi$ at each sequence $j \in [1, N]$. For a given N we introduce $\mathbb{C} = \sum_{j=1}^N p_2(j)$, which essentially quantifies cumulatively the unfavorably absorption events. In Fig. 14, the black curve corresponds to the cumulative probability with which photons can get absorbed in a projective measurement protocol and the blue curve corresponds to the total probability obtained by adding the population of level $|2\rangle$ at the end of each B-pulse in the coherent measurement protocol. It is clearly seen that the coherent measurement protocol has lesser cumulative net probability of B-pulse absorption.

Identical and random pulses

Let us have a closer look at the simulation in the case of N B-pulses with equal and with unequal (random) pulse strengths. In Fig. 15, circular markers present the case of $N \in [1, 25]$ B-pulses with equal strengths and triangular markers correspond to randomly chosen B-pulse

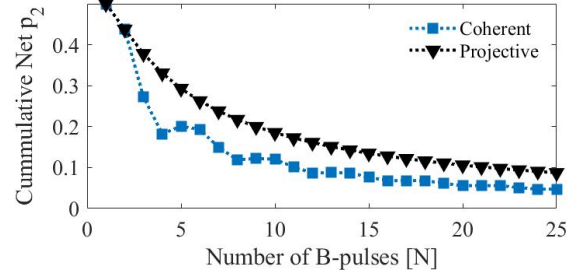


FIG. 14. Cummulative probability \mathbb{C} of B-pulse absorption with $\theta = \pi$ versus N . Blue dotted curve with square markers corresponds to the case of coherent interaction-free measurement protocol and black dotted curve with triangular markers results from projective measurement protocol.

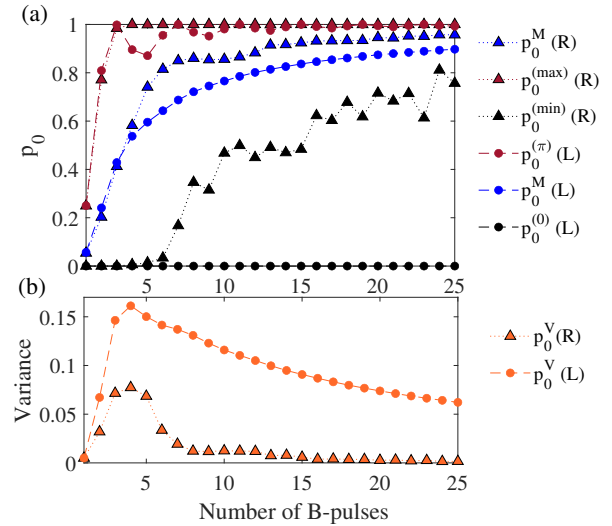


FIG. 15. (a) Mean and extreme values of p_0 are plotted for $N \in [1, 25]$ for the cases of identical B-pulses ($\theta_i = \theta_j = \theta$ $i, j \in [1, N]$) as θ varies linearly from 0 to π for each N with circular markers. Triangular markers present the corresponding results when $\theta_i \neq \theta_j$ and each θ_i is chosen arbitrarily from $[0, \pi]$ independent of any θ_j . $p_0^M(L)$, $p_0^{(0)}(L)$, and $p_0^{(\pi)}(L)$ are mean, minimum and maximum values respectively of the p_0 distribution for the case of identical B-pulses with linearly varying strengths. $p_0^M(R)$, $p_0^{(min)}(R)$, and $p_0^{(max)}(R)$ are mean, worst and best values respectively from the p_0 distribution for the case of random B-pulse strengths. (b) Curves showing the corresponding variance of the p_0 distributions with N .

strengths. In this case, the strengths θ of each B-pulse increase linearly from 0 to π in 400 steps and the resulting distributions of the ground state population p_0 is obtained. As expected, in Fig. 15(a) the black circles connected by dashed black line representing the case of no B-pulses yield $p_0 = 0$, while the dashed line with red circular markers corresponds to $\theta = \pi$, which has a tendency to stay closer to 1. We note that $\theta = \pi$ may not correspond to maximum value of p_0 especially for smaller values of N . In fact the maximum p_0 in both cases (equal and unequal

B-pulse strengths) coincide with each other and is represented by red triangles. The average value of ground state population ($p_0^M(L)$) in the case of linearly varying θ gradually increases from 0.057 for $N = 1$ to 0.897 for $N = 25$ as shown with blue dashed curve with circles. Interestingly, the situation with randomly chosen $\theta \in [0, \pi]$ (400 samples for each N), gives rise to higher average values ($p_0^M(R)$) as shown with blue dotted curve with triangular markers. Black and red dotted curves with triangular markers result from the worst and best combinations of random B-pulses. It is noteworthy that even the worst choice of random B-pulses have a good chance of being detected. While the ignorance about the B-pulse strengths appear to benefit in this case, results from randomly chosen B-pulse strengths also depend upon the sample size (here the sample size is 400). Further, variance of the p_0 distributions for each N is shown in Fig. 15(b), where circular markers correspond to the case of equal B-pulse strengths and triangular markers correspond to the case of random B-pulse strengths. Much lower values of variance are obtained in the case of arbitrarily chosen B-pulse strengths.

SUPPLEMENTARY NOTE 4: DISCUSSION: IGNORANCE IS BLISS

The previous numerical simulations demonstrate that the coherent case is more efficient than the standard projective (quantum Zeno effect) case. This is a non-intuitive result, because negative measurements, while not producing any macroscopic event (detector click, etc.) still provide more information. A famous example outside quantum physics is the Monty Hall problem.

However, the strategy of extracting “classical” information is not necessarily advantageous, as the case of coherent interaction-free detection realized in this paper show. To give a qualitative justification of why it is so, let us consider the state $\sqrt{1-x^2-y^2}|0\rangle + x|1\rangle + y|2\rangle$ at the input of a Ramsey segment containing the pulse $B(\pi)$. After going through the interferometer the population p_2 on state $|2\rangle$ is $\left[\sqrt{1-x^2-y^2}\sin(\pi/2(N+1)) + x\cos(\pi/2(N+1))\right]^2$. Let’s examine now the projective scenario. In this case, the input state should not contain any component on the state $|2\rangle$, since in this protocol the state is always projected on the $\{|0\rangle, |1\rangle\}$ subspace. Considering $\sqrt{1-x^2}|0\rangle + x|1\rangle$ as the input state, we find that the probability of detection (“explosion”) is $\left[\sqrt{1-x^2}\sin(\pi/2(N+1)) + x\cos(\pi/2(N+1))\right]^2$, clearly larger than in the coherent case.

SUPPLEMENTARY NOTE 5: EXPERIMENTAL ERRORS DUE TO PULSE IMPERFECTIONS

We present here an analysis of errors due to the imperfect generation of pulses in our setup. These imperfections are: IQ mixer saturation, finite sampling rates, detunings with respect to the corresponding transition frequencies, etc. For example, IQ mixer saturation effects start to be observable in our setup for values $\theta > 3\pi$ (approximately); at the highest power, a pulse with amplitude $\Omega_0(4\pi)$ in fact implements a unitary with $\theta = 3.9\pi$. These imperfections are embedded in our simulations.

To characterize these errors we obtain the explicit form of the unitary evolution generated by the drive Hamiltonian in Eq. 3 (from the main text) and compare it with the ideal beam-splitter unitaries S_1 (Eq. 6), S_2 (Eq. 19), and the B-pulses $B(\theta)$ (Eq. 7). The Hamiltonian in Eq. 3 (from the main text) generates a unitary evolution, and the corresponding dynamics can be determined by solving

$$i\hbar \frac{\partial}{\partial t} |\psi(t)\rangle = H(t) |\psi(t)\rangle, \quad (46)$$

where $|\psi(t)\rangle$ is the state of the system at an arbitrary time t and $\Omega_{01}(t)$ ($\Omega_{12}(t)$) are the drives from Eq. 1 (main text). Following Eq. (46), we obtain the dynamics of our three-level system initialized in the computational basis states $|0\rangle$, $|1\rangle$, and $|2\rangle$. Each of these states undergo the same evolution for the same time, resulting in states $|\psi_0(t)\rangle$, $|\psi_1(t)\rangle$, and $|\psi_2(t)\rangle$ respectively. The explicit form of the corresponding unitary operator at arbitrary time t can thus be written as

$$U_{\text{sim}}(t) = |\psi_0(t)\rangle\langle 0| + |\psi_1(t)\rangle\langle 1| + |\psi_2(t)\rangle\langle 2|. \quad (47)$$

This unitary operator is obtained numerically for given experimental parameters. Numerical integration is performed using the fourth-order Runge-Kutta method with a step size of (AWG sampling rate) $^{-1}$. Thus, the super-Gaussian pulse envelope of 56 ns duration is discretized by the AWG sampling rate of 1 GS/s. Deviation of U_{sim} from the ideally expected $U(t)$ ($= S_1$ or S_2 or $B(\theta)$) is calculated using the 2-norm of the difference between the operators, given by $\xi = \|U(t) - U_{\text{sim}}(t)\|_2$. Note that the maximum value of ξ is 2. Thus we can quantitatively assess each individual unitary operation implemented in the experiments. We have also analyzed the results of single-qutrit quantum process tomography (QPT) [34, 35] and obtained the precision of the overall pulse sequence ($S_1 B(\theta) S_1$). Process matrices (χ_{sim}) resulting from the simulation (without decoherence) including pulse errors are compared with that of the ideal process matrix (χ_{ideal}) using the fidelity measure $\mathcal{F} = [\text{Tr} \sqrt{\sqrt{\chi_{\text{ideal}}} \chi_{\text{sim}} \sqrt{\chi_{\text{ideal}}}}]^2$.

Overall, this analysis results in the following bounds for the errors. For $N = 1$ the beam-splitter unitary S_1 has $\xi = 0.01$ and the average ξ for $B(\theta)$ is 0.06. From tomography, $\mathcal{F} = 0.98$, averaged over $\theta \in [0, 4\pi]$. For $N = 2$, we

have $\xi = 0.07$ for S_2 and average $\xi = 0.21$ for $B(\theta)$. Further, evaluating the whole process $(S_2 B(\theta) S_2 B(\theta) S_2)$ via QPT, we obtain an average fidelity $\mathcal{F} = 0.91$. Results from the simulations with these pulse errors alongside with decoherence match the experimental datasets quite well as shown in Figs. (2,3) of the main text and Fig. (10) of this supplementary material.

SUPPLEMENTARY NOTE 6: REPRESENTATION ON THE MAJORANA SPHERE

Geometrical representations are useful for understanding quantum operations. Here we adopt the Majorana representation to visualize geometrically the single-qutrit dynamics during our protocol. We simulate the single-qutrit dynamics on the Majorana sphere for the case of multiple consecutive MZI setups,

In the Majorana geometrical representation, a particle with spin j is represented by $2j$ points (known as the Majorana stars) on a unit sphere (known as the Majorana sphere). Consider an arbitrary state of a spin j particle in the $|jm\rangle$ basis,

$$|\Psi\rangle = \sum_{m=-j}^j c_m |jm\rangle, \quad (48)$$

where c_m are the complex coefficients. The corresponding Majorana polynomial of degree $2j$ is constructed as $P_{|\Psi\rangle}(\zeta) = a_0 \zeta^{2j} + a_1 \zeta^{2j-1} + \dots + a_{2j}$, with

$$a_r = (-1)^r \frac{c_{j-r}}{\sqrt{r!} \sqrt{(2j-r)!}}. \quad (49)$$

$P_{|\Psi\rangle}(\zeta) = 0$ has $2j$ roots, which can be plotted in the xOy plane. The inverse stereographic projections of each of these points with respect to the South Pole of the unit sphere give rise to Majorana stars (S_i , $i \in [1, 2j]$). Thus, the Majorana representation of a qutrit ($j = 1$) consists of two Majorana stars. For $j = 1$ we have $m = -1, 0, 1$, and the qutrit basis $|0\rangle$, $|1\rangle$, $|2\rangle$ may be identified as $|1m\rangle \equiv |1-m\rangle$. For the state $|0\rangle$ both Majorana stars lie on the North Pole, $|2\rangle$ has both Majorana stars lying on the South Pole, while $|1\rangle$ is represented by one Majorana star on the North Pole and another one on the South Pole.

First, we consider a single Ramsey setup. We initialize a qutrit in the state $|0\rangle$ and simulate the pulse sequence for $\theta_1 = 0, \pi$. The corresponding quantum state dynamics is calculated and plotted as a dynamics of Majorana stars in Figure 16. Figs. 16(a1),(a2),(a3) present the trajectory under the first beam splitter, during the evolution in the absence of a pulse, and respectively under the second beam splitter. The Majorana stars $S_1(x_1, y_1, z_1)$ and $S_2(x_2, y_2, z_2)$ are shown in red and blue colors, where x_i, y_i, z_i are Cartesian coordinates. To begin with, both stars lie at the North Pole, corresponding to the state

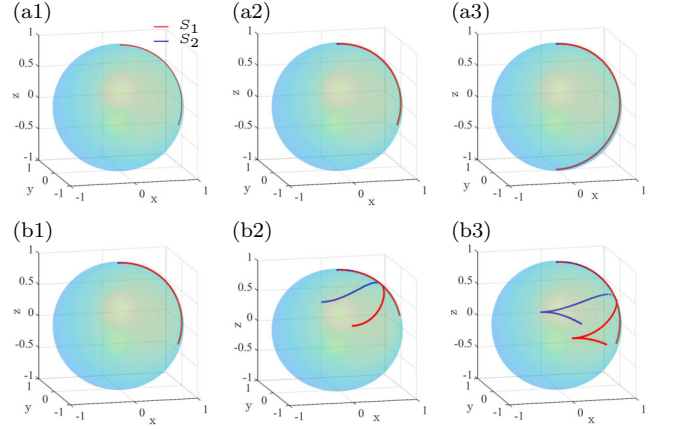


FIG. 16. Majorana trajectories at each step in the single Ramsey protocol without a pulse (a1)-(a2)-(a3) and with a pulse (b1)-(b2)-(b3) using a three-level quantum system.

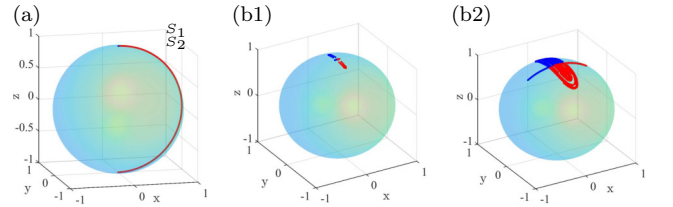


FIG. 17. Majorana trajectories resulting from the emulation of N consecutive MZI setups with Ramsey angles $\pi/(N+1)$. The subplots correspond to: (a) no pulse, (b1) $N = 100$ with 100 equal-strength pulses ($\theta_j = \pi$), and (b2) $N = 100$ with 100 pulses ($\theta_j = \text{random}$).

$|0\rangle$. Under the effect of the first beam splitter, the Majorana star S_1 moves in the plane $y = 0$, while S_2 stays at the North Pole such that the qutrit attains the state: $(|0\rangle + |1\rangle)/\sqrt{2} + |2\rangle$, see Fig. 16(a1). Further, since there is no bomb in this case, no change is observed in Fig. 16(a2). Finally, the second beam splitter brings S_1 to the South Pole of the sphere, see Fig. 16(a3), thus representing the state $|1\rangle$ (one star at the north pole, one star at the south pole). The corresponding trajectories for $\theta_1 = \pi$ are shown in Figure 16(b1),(b2),(b3). These two cases with $\theta_1 = 0, \pi$ are clearly distinct as observed from Figs. 16(a2) and (b2). Fig. 16(b2) shows a non-trivial trajectory, in which S_1 partially retraces its path very quickly and in the meantime S_2 moves along the previous trajectory of S_1 such that both of these Majorana stars meet somewhere in the middle of the trajectory and then start moving symmetrically in different directions. This step corresponds to the generation of the coherence between states $|0\rangle$ and $|2\rangle$. Finally, the last step implements the same beam splitter again, leading to the state $(|0\rangle + |1\rangle)/2 + |2\rangle/\sqrt{2}$ with Majorana stars $S_1(0.586, 0.792, -0.172)$ and $S_2(0.586, -0.792, -0.172)$. Clearly, the case $\theta \neq 0$ and $\theta = \pi$ are distinguishable by the different star constellations.

Next, we go ahead with this geometrical picture and observe the single qutrit dynamics with multiple pulses. For $N=2$, with $\theta_1 = \theta_2 = \pi$, we find that the coordinates of the final state Majorana stars are $(0.062, \pm 0.935, 0.350)$. For $N \geq 2$, both the Majorana stars end up in the northern hemisphere. Figs. 17(a-b1-b2) present the final states obtained in the case of no pulse, 100 pulses with equal $\theta_j = \pi$, and 100 pulses with randomly chosen θ_j 's respectively. As discussed earlier, the case of no pulse corresponds to the Majorana stars $S_1(0, 0, -1)$ and $S_2(0, 0, 1)$.

The final state of the single-qutrit emulating 100 consecutive Ramsey setups with 100 pulses is confined to the region around the North Pole, see Figs. 17(b1-b2). Thus

a completely contrasting configuration of the Majorana stars is observed for the case of no pulse versus the case with many pulses (here 100). Thus it is clear from the Majorana geometrical representation that for the case of large number of pulses, the probability of interaction-free detection is quite high and that the bomb strength does not matter anymore.

To conclude, we obtained the signature of coherent interaction free detection on the Majorana sphere. The results obtained from the single qutrit dynamics on the Majorana sphere is in complete agreement with the theoretical expectations and simulations.